Manipulating Femtosecond Spin–Orbit Torques with Laser Pulse Sequences to Control Magnetic Memory States and Ringing

P. C. Lingos[1], J. Wang[3], and I. E. Perakis[1,2]
[1]*Department of Physics, University of Crete, Box 2208, Heraklion, Crete, 71003, Greece*
[2]*Institute of Electronic Structure & Laser, Foundation for Research and Technology-Hellas, Heraklion, Crete, 71110, Greece and*
[3]*Ames Laboratory and Department of Physics and Astronomy, Iowa State University, Ames, Iowa 50010, USA*
(Dated: September 13, 2021)

Femtosecond (fs) coherent control of collective order parameters is important for non–equilibrium phase dynamics in correlated materials. Here we propose a possible scheme for fs control of a ferromagnetic order parameter based on non–adiabatic optical manipulation of electron–hole (e–h) photoexcitations between spin–orbit–coupled bands that are exchange–split by magnetic interaction with local spins. We photoexcite fs carrier spin–pulses with controllable direction and time profile without using circularly–polarized light, via time–reversal symmetry–breaking by non–perturbative interplay between spin–orbit and magnetic exchange coupling of coherent photocarriers. We manipulate photoexcited *fs spin–orbit torques* to control complex switching pathways of the magnetization between multiple magnetic memory states. We calculate the photoinduced fs magnetic anisotropy in the time domain by using density matrix equations of motion rather than the quasi–equilibrium free energy. By comparing to pump–probe experiments, we identify a "sudden" magnetization canting induced by laser excitation, which displays magnetic hysteresis absent in static magneto–optical measurements and agrees with switchings measured by Hall magnetoresistivity. The fs magnetization canting switches direction with magnetic state and laser frequency, which distinguishes it from nonlinear optical and demagnetization longitudinal effects. By shaping two–color laser–pulse sequences analogous to multi–dimensional Nuclear Magnetic Resonance (NMR) spectroscopy, we show that sequences of clockwise or counter–clockwise fs spin–orbit torques can enhance or suppress magnetic ringing and switching rotation at any desired time. We propose protocols that can provide controlled access to four magnetic states via consequative 90° switchings.

PACS numbers: 78.47.J-, 75.50.Pp, 75.30.Hx, 75.78.Jp

arXiv:1411.6662v1 [cond-mat.str-el] 24 Nov 2014

I. INTRODUCTION

Femtosecond (fs) control of switching between condensed matter states[1–4] may address challenges posed by multi–functional devices for information storage and processing on a single chip at up–to–thousand–times faster terahertz speeds. One of the main obstacles for widespread use of magnetic materials in such applications is the lack of efficient control of magnetization. Fast spin manipulation is one of the main challenges for spin-electronics, spin–photonics, magnetic storage, and quantum computation.[5] To meet this challenge, different magnetic systems must be explored. In diverse systems ranging from ferromagnetic semiconductors[6–8] to doped topological insulators,[9,10] magnetic effects arise from exchange interactions ($\propto \mathbf{S}\cdot\mathbf{s}$) between two distinct sub–systems: mobile, spin–orbit–coupled electron spins ($\mathbf{s}$) and magnetic local moments ($\mathbf{S}$).[11] These interactions couple, for example, magnetic impurity spins with Dirac fermions in topological insulators[9] or valence–band holes in (III,Mn)V semiconductors.[6] Such couplings break time–reversal symmetry and resut in ferromagnetic states with two distinct but strongly–coupled collective–spin order parameter components.[6,9] When brought out of thermodynamic equilibrium, interacting mobile and local collective spins allow more "knobs" for manipulating ultrafast magnetism[12] by using fs laser pulses.

As is known in both semiconductors[13–17] and metals,[18–20] depending on the timescale, a distinction must be made between e–h quantum excitations, non–thermal e and h populations, and Fermi–Dirac populations (see the schematic in Fig. 1(a)). Initially, only coherent e–h pairs are photoexcited (left part of Fig. 1(a)). At a second stage, scattering events lead to the decay of these quantum excitations within a time–interval T_2. When T_2<100fs, such dephasing occurs during the laser pulse and the treatment of e–h coherence is necessary only for describing the nonlinear fs photoexcitation processes. The contribution of e and h populations of the photoexcited states is important when their relaxation/thermalization time T_1 is not too short compared to the ∼100fs timescales of interest.[18] Such non–thermal populations redistribute between the band states as they relax into hot Fermi–Dirac distributions within T_1 (Fig. 1(a)).[18] This relaxation occurs after picosecond (ps) times (via emission of multiple phonons) or faster (10's to 100's of fs via Coulomb interactions).

While the quantum kinetics of charge photoexcitations is well–studied,[13,18] fs non–adiabatic magnetic correlation is not well–understood.[1,3,4,21] Collective spin dynamics is triggered when coupled magnetic order parameter components are "suddenly" brought out of equilibrium during coherent photoexcitation. Photoinduced coherent, non–thermal, and hot–Fermi–Dirac mobile carrier spins interact with the collective local spin during ultra–short timescales. Their relative contributions depend on laser intensity and frequency, relaxation parameters, material properties, and probed timescales.

Pulse–shaping[22] and sequences of fs laser–pulses analogous to multidimensional NMR spectroscopy[15,23] offer additional possibilities for clarifying and controlling such transient magnetic response. Here we show that coherent optical control of non–equilibrium mobile carrier spin induced by non–thermal population imbalance can suppress or start magnetization ringing or switching rotation at any time, by exerting *fs spin–orbit torque* sequences in the appropriate directions. In this non–adiabatic way, we can control magnetic states without relying on magnetic field pulses, circularly–polarized light,[17,24,25] demagnetization,[8,26–28] precession phase,[37] or quasi–thermal processes.[2,29–32]

The fs photoexcitation of (Ga,Mn)As has revealed different transient magneto–optical responses, such as ultrafast increase (decrease) of magnetization amplitude under weak (strong) excitation[8,27,33] and magnetization re–orientation due to spin–torque[17,25] and spin–orbit torque.[3,34,35] There is mounting evidence that non–thermal magnetic processes play an important role in the fs magnetization time evolution.[3,17,34,35] Such (III,Mn)V heterostructures are advantageous for optical control of magnetic order due to their well–characterized optical and electronic properties and manipulable carrier–induced ferromagnetism. Useful for demonstrating our theoretical predictions is that these systems have four different in-plane magnetic states (X^+, Y^+, X^-, and Y^-) due to bi–axial magnetic anisotropy between the [100] and [010] crystallographic axes (Fig. 1(b) and Appendix A). While in conventional ferromagnets switching involves spin–flipping between two magnetic states (spin–up/spin–down), the existence of four magnetic states allows for more complex multi–state switching pathways. Their experimental observation can validate more elaborate magnetization coherent control schemes, such as the one proposed here. Four–state magnetic memories are also useful for ultra–high–density magnetic recording. Two equivalent easy axes double the recording density, by recording two bits of information on the same spot.[36] To take advantage of multi–state magnetic memories for ultrafast spintronics applications, we must be able to selectively access all magnetic states in any desired sequence. There is no generally accepted scheme for this. However, optical spin manipulation has already reached a high level of sophistication[3,8,17,24,32,34,36–41] and control of magnetization on a 100ps timescale has been demonstrated in various systems, by using magnetic field or laser–generated magnetic pulses[42–44] or photoinduced effects.[2,45] Two outstanding challenges have to be better addressed: (i) how to initiate and stop controlled deterministic switchings during fs time intervals, (ii) how to suppress the magnetic ringing associated with switchings, which limits the prospects for high–speed applications.[46] From a more general perspective, the dynamical disentanglement of degrees of freedom that are strong–coupled in equilibrium, e.g. the mobile and local collective spin sub–systems studied here, may lead to a better understanding of correlated systems.[1,4,47,48] The advantage of using spin–charge quantum kinetics to overcome the limitations of incoherent processes for meeting the above challenges is now beginning to be recognized.[1,3,4,17,40,41,49,50]

This work contributes to the debate of how fs coherent photoexcitation could drive and control ultrafast switchings[1,12] and magnetic ringing.[46] We consider the very early non–thermal and coherent temporal regimes and focus mostly on magnetization changes *during the fs laser pulse*. We show that, by choosing appropriate sequences of time–delayed laser pulses, we can control the direction, magnitude, and time–profile of the short–lived non–thermal photocarrier spin. The latter drives the magnetization away from equilibrium by exerting fs spin–orbit torque on the collective local spin. By coherent manipulation of the e–h photoexcitations, we photogenerate a controlled population imbalance between spin–orbit–coupled/exchange–split bands. Such photoexcited band carrier population and spin imbalance is not restricted by the chemical potential or temperature and leads to a fully controllable "sudden" magnetization canting in selected directions at desirable times. Based on direct control of the above non–thermal processes by the optical field, we propose possible protocols that drive complex 360° magnetization pathways involving sequential 90° deterministic switchings between *four different* magnetic memory states. Such spin control, as well as suppression of both magnetic ringing and switching rotations, are possible without circularly–polarized light due to relativistic spin–orbit coupling of the photocarriers. For linearly–polarized fs optical pulses, we show that the photoexcited carrier spin direction and amplitude is determined by the competition between spin–orbit coupling with characteristic energy $\Delta_{so}\sim$340meV given by the Γ–point energy splitting of the GaAs spin–orbit–split valence band, and the $\mathbf{S}\cdot\mathbf{s}$ magnetic exchange coupling, with characteristic energy $\Delta_{pd}=\beta c S\sim$100meV in Ga(Mn)As,[6] where S and c denote the Mn spin amplitude and concentration respectively and β is the magnetic exchange constant. The time–reversal symmetry breaking can be characterized by the energy ratio $\Delta_{pd}/\Delta_{so}(\sim 1/3$ in (Ga,Mn)As). It leads to fs photoexcitation of short–lived mobile spin–pulses ($\mathbf{s}$), whose direction is controlled by selectively populating the continua of exchange–split heavy–hole (HH) or light–hole (LH) spin–orbit–coupled band states with different spin superpositions. We model the fs nonlinear photoexcitation processes, driven by sequences of time–delayed laser–pulse–trains, with density matrix equations–of–motion[13] describing carrier populations coupled non–perturbatively to inter–band coherences and local spins. Our time–domain calculations describe a non–equilibrium magnetic anisotropy during the laser pulse, which we estimate by treating strong band non–parabolicity and spin–orbit couplings using the tight–binding bandstructure of GaAs with mean–field magnetic exchange interaction.[6,51] We relate the calculated coherent photoexcitation of fs spin–orbit torque to existing experiments and make predictions for new ones

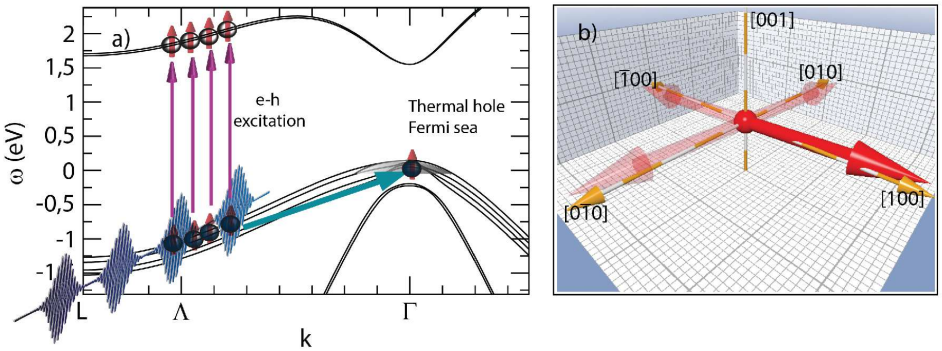

FIG. 1: (Color online) (a): Schematic of two contributions to the transient magnetic anisotropy: e–h excitations (non–thermal and coherent carrier contribution, left part) and Fermi sea holes (thermal contribution, right part). For $\hbar\omega_p$∼3.1eV, the holes are excited in high–$\mathbf{k}$, non–parabolic, HH or LH exchange–split valence band states. (b): The thermal hole Fermi sea free energy gives four in–plane magnetic memory states X^+, Y^+, X^-, and Y^-, slightly tilted from the corresponding crystallographic axes.

to observe switchings by using pulse–shaping.[22]

The paper is organized as follows. In Section II we discuss the symmetry–breaking processes leading to photoexcitation of a 100fs mobile carrier spin–pulse with direction and magnitude that depend on the ratio Δ_{pd}/Δ_{so}. In Section III we compare theory and experiment to demonstrate coherent control of fs spin–orbit torque direction and magnitude by tuning populations of four exchange–split HH and LH valence bands excited by a laser pulse. We show that the canting direction of a transverse, out–of–plane, fs magnetization component displays a magnetic hysteresis absent without pump, which is distinguished from longitudinal amplitude and nonlinear optical effects by sweeping a perpendicular magnetic field. In Section IV we show that we can initiate controlled switching rotations to any one of the available magnetic states by shaping a laser–pulse train. In Section V we propose two protocols for controlling four sequential 90° switchings in clockwise or counter–clockwise directions. In Section VI we use two time–delayed laser–pulse–trains to suppress or enhance the nonlinear switching rotation at any intermediate state and to suppress magnetic ringing at any time, long or short. Rather than relying on the magnetization precession phase, we achieve this coherent control by switching the *directions* of fs spin–orbit torques. We end with conclusions and a broader outlook. In two Appendices we present the density matrix equations describing nonlinear coherent excitation of fs spin–orbit torque, separate non–adiabatic/non–thermal and adiabatic/thermal transient magnetic anisotropy, and treat the non–parabolic and anisotropic spin–orbit–coupled band continua.

II. FEMTOSECOND SPIN PHOTOEXCITATION

In this section we discuss the general processes leading to photoexcitation of carrier spin with direction determined by non–perturbative symmetry–breaking interactions. In the systems of interest, the magnetic effects arise from antiferromagnetic interactions between localized and mobile (delocalized) carrier spins.[6] In contrast to magnetic insulators studied before,[24] the localized electrons do not contribute to the fs magnetic anisotropy. They determine the magnetization (collective local spin)

$$\mathbf{S} = \frac{1}{cV}\sum_i \langle \hat{\mathbf{S}}_i \rangle, \tag{1}$$

where V is the volume and $\mathbf{S}_i$ are the local magnetic moments at positions i, with concentration c. For example, in (III,Mn)V magnetic semiconductors, the local magnetic moments are pure S=5/2 Mn spins with zero angular momentum, L=0, and no spin–orbit interaction. The fs magnetic anisotropy comes from band electrons that are subject to spin–orbit interactions and, unlike for the localized electrons, couple directly to light. The spin–exchange coupling of such photoexcited itinerant carriers with the local spins results in photoinduced magnetization dynamics. The widely–used mean–field treatment of the magnetic exchange interaction (Zener model) captures the symmetry–breaking of interest here.[6] We thus consider the dynamics of a single–domain macrospin $\mathbf{S}$(t) and neglect spatial fluctuations.[39,40] This approximation describes metallic–like (III,Mn)V and other magnetic semiconductors.[6]

Our main goal here is to control the non–equilibrium spin of band carriers in order to manipulate the magnetization motion. These non–equilibrium carriers dominate the laser–induced magnetization changes during fs timescales. While spin–lattice coupling affects the easy axis, lattice heating and relaxation occurs on ps timescales, following energy transfer from electronic system of interest here.[32,35] The laser excites e–h pairs between the different exchange–split valence and conduction bands (Fig. 1(a)). Magnetic exchange mainly involves the valence hole collective spin $\mathbf{s}_h$. Denoting by

$\mathbf{s}^h_{\mathbf{k}n}$ the contribution of valence band n with given $\mathbf{k}$,

$$\mathbf{s}_h(t) = \frac{1}{V}\sum_{\mathbf{k}}\sum_{n}\mathbf{s}^h_{\mathbf{k}n}(t). \quad (2)$$

We want to control $\mathbf{s}^h_{\mathbf{k}n}(t)$ between different bands. We describe this spin by extending the discrete–$\mathbf{k}$ calculation of fs spin–orbit–torque in Ref.[3] to include the anisotropic continua of non–parabolic (Ga,Mn)As bands and to consider sequences of laser–pulse–trains. We can thus estimate the photocarrier density and net spin as function of laser–pulse frequency, intensity, and time delays for comparisons to experiments. The mechanism of Ref.[3] is analogous to the current–induced spin–orbit torque[52] observed in (Ga,Mn)As[53] and other spin–orbit–coupled ferromagnets. Unlike in our earlier work[17] on fs spin–transfer torque analogous to the one induced by spin–polarized currents in spintronics applications,[54,55] which is observed experimentally by using circularly–polarized light,[25] here spin is not conserved due to the spin–orbit coupling. As a result, angular momentum transfer from the photons is not necessary due to the symmetry–breaking provided by the competition of spin–orbit and magnetic exchange couplings.

To initiate ultrafast dynamics, we create a short–lived spin imbalance by optically controlling the individual contributions $\mathbf{s}^h_{\mathbf{k}n}$(t) of different electronic bands and Brillouin zone directions. To describe this, we express the mobile carrier spin in terms of the electronic density matrix $\langle\hat{h}^\dagger_{-\mathbf{k}n}\hat{h}_{-\mathbf{k}n'}\rangle$, defined in terms of an adiabatic basis of band eigenstates created by the operators $\hat{h}^\dagger_{-\mathbf{k}n}$:

$$\mathbf{s}^h_{\mathbf{k}n} = \hat{\mathbf{s}}^h_{\mathbf{k}nn}\,\langle\hat{h}^\dagger_{-\mathbf{k}n}\hat{h}_{-\mathbf{k}n}\rangle + \sum_{n'\neq n}\hat{\mathbf{s}}^h_{\mathbf{k}nn'}\,\langle\hat{h}^\dagger_{-\mathbf{k}n}\hat{h}_{-\mathbf{k}n'}\rangle, \quad (3)$$

where $\hat{\mathbf{s}}^h_{\mathbf{k}n'n}$ are the spin matrix elements. These describe the spin direction of carriers populating band states $(n,\mathbf{k})$. Spin direction changes for different $\mathbf{k}$–direction and band. It is determined by spin–mixing due to non–perturbative interplay of spin–orbit and magnetic exchange couplings, which depends on Δ_{pd}/Δ_{so}. The first term on the right hand side (rhs) of Eq.(3) describes the population contribution (coherent, non–thermal, or quasi–thermal). The second term descibes the contribution due to coherent coupling of different bands (inter–valence–band coherence). Such Raman coherence arises because spin is not conserved, $\hat{\mathbf{s}}^h_{\mathbf{k}nn'}\neq 0$, and vanishes in equilibrium. We choose as basis $\hat{h}^\dagger_{-\mathbf{k}n}$ the eigenstates (n,$\mathbf{k}$) of the adiabatic Hamiltonian (Appendix A)

$$H_b(\mathbf{S}) = H_0 + H_{so} + H_{pd}(\mathbf{S}_0). \quad (4)$$

H_0+H_{so} describes the bandstructure of the parent material (undoped GaAs here), due to the periodic lattice potential (H_0) and the spin–orbit coupling (H_{so}).[51] The symmetry–breaking is induced by the magnetic exchange interaction $H_{pd}(\mathbf{S}_0)$, Eq.(A1).[6] Here, $\mathbf{S}_0$ denotes the slowly–varying contribution to the local macrospin, which switches or oscillates during ps timescales (adiabatic approximation). The valence hole and conduction electron basis states, $\hat{h}^\dagger_{-\mathbf{k}n}$ and $\hat{e}^\dagger_{\mathbf{k}m}$ respectively, were obtained by diagonalizing $H_b(\mathbf{S}_0)$ using the tight–binding approximation of Ref.[51] (Appendix A).

In (III,Mn)V semiconductors, a thermal hole Fermi sea bath, characterized by the Fermi–Dirac distribution $f_{n\mathbf{k}}$, is already present in the ground state (Fig. 1(a)).[6] Similar to ultrafast studies of the electron gas in metals[18] and semiconductors,[56,57] we distinguish this quasi–equilibrium contribution to Eq.(3) from the non–Fermi–Dirac femtosecond contribution (Appendix A):

$$\langle\hat{h}^\dagger_{\mathbf{k}n}\hat{h}_{\mathbf{k}n'}\rangle = \delta_{nn'}f_{n\mathbf{k}} + \Delta\langle\hat{h}^\dagger_{\mathbf{k}n}\hat{h}_{\mathbf{k}n'}\rangle. \quad (5)$$

At quasi–equilibrium, only the Fermi–Dirac populations contribute. These are characterized by a temperature and chemical potential and give the adiabatic field[6,24,35]

$$\gamma\mathbf{H}_{FS}[\mathbf{S}] = -\frac{\partial E_h(\mathbf{S})}{\partial\mathbf{S}}, \quad (6)$$

where γ is the gyromagnetic ratio and

$$E_h(\mathbf{S}) = \sum_{\mathbf{k}n}\varepsilon^v_{n\mathbf{k}}\,f_{n\mathbf{k}} \quad (7)$$

is the total (free) energy of the relaxed Fermi–Dirac carriers. $\varepsilon^v_{n\mathbf{k}}(\mathbf{S})$ are the (valence band) eigenvalues of the adiabatic Hamiltonian H_b for frozen local spin $\mathbf{S}$. The above adiabatic free energy of the mobile hole Fermi sea defines the magnetic memory states of Fig. 1(b) (Appendix A). Since the changes of E_h with $\mathbf{S}$ are notoriously small for numerical calculations of the quasi–equilibrium magnetic anisotropy,[35,58] while the low–energy states of (III,Mn)V systems are complicated by sample–dependent disorder, impurity bands, defect states, and strain,[6,27,38,59] we approximate $E_h(\mathbf{S})$ by using the symmetry–based Eq.(A9) with parameters extracted from experiment (Appendix A).[6,38,59] In this way, we introduce the realistic four–state magnetic memory of the (III,Mn)V materials. For the low 10–100$\mu J/\mathrm{cm}^2$ pump fluences considered here, we neglect any laser–induced changes in the Fermi–Dirac distribution temperature and chemical potential, which add to the predicted effects on the timescale of energy and population relaxation. Previous calculations assuming Fermi–Dirac distributions[27,35] gave order–of–magnitude smaller magnetization dynamics compared to experiment and concluded that the non–equilibrium hole distribution is very broad.[27] Here we study the possible role of the short–lived (∼10–100fs) non–Fermi–Dirac populations that exist prior to full electronic thermalization. We calculate such fs anisotropy in the time domain, by solving equations of motion for $\Delta\langle\hat{h}^\dagger_{\mathbf{k}n}\hat{h}_{\mathbf{k}n'}\rangle$ using the time–dependent Hamiltonian (Appendix A)

$$H(t) = H_b(\mathbf{S}_0) + \Delta H_{exch}(t) + H_L(t). \quad (8)$$

While $H_b(\mathbf{S}_0)$ changes during 10's of ps, the other two contributions to Eq.(8) are non–adiabatic and vary during fs timescales. $H_L(t)$, Eq. (A3), describes the dipole

coupling of the fs laser E–field,[13] while

$$\Delta H_{exch}(t) = \frac{1}{V}\sum_{\mathbf{k}} \beta_{\mathbf{k}} c\, \Delta\mathbf{S}(t)\cdot \hat{s}^h_{\mathbf{k}}, \quad (9)$$

where $\hat{s}^h_{\mathbf{k}}$ is the hole spin operator and

$$\Delta\mathbf{S}(t) = \mathbf{S}(t) - \mathbf{S}_0. \quad (10)$$

describes "sudden" changes in magnetization during fs photoexcitation. We assume exchange constant $\beta_{\mathbf{k}}\approx\beta$ for simplicity within the relevant range of $\mathbf{k}$. The effects of non–adiabatic $\Delta\mathbf{S}$(t) on the time–dependent band states are described via the density matrix equations of motion.

We describe the non–Fermi–Dirac electronic contribution $\Delta\langle\hat{h}^\dagger_{\mathbf{k}n}\hat{h}_{\mathbf{k}n'}\rangle$, Eq.(5), similar to the well–established Semiconductor Bloch Equation[13,60] or local–field[16,61] Hartree–Fock treatments of ultrafast nonlinear optical response. In particular, we solve coupled equations of motion for the electronic populations and inter–band coherences $\langle\hat{h}^\dagger_{\mathbf{k}m}\hat{h}_{\mathbf{k}n}\rangle$, $\langle\hat{e}^\dagger_{\mathbf{k}m}\hat{e}_{\mathbf{k}n}\rangle$, and $\langle\hat{e}_{\mathbf{k}m}\hat{h}_{-\mathbf{k}n}\rangle$ that are non–perturbatively coupled to the time–dependent local spin $\mathbf{S}$(t). This coupling modifies the electronic dynamics, which, in turn, modifies the motion of $\mathbf{S}$(t) (Appendix A). We consider linearly–polarized optical pulses with zero angular momentum. We do not include the carrier-carrier, carrier-phonon, and carrier–impurity interactions in the Hamiltonian, but treat the photocarrier relaxation phenomenologically, by introducing e–h lifetimes (dephasing time T_2) and non–thermal population relaxation times T_1. Our calculation thus describes the "initial condition" that brings the system out of equilibrium and initiates relaxation.[27,50] The latter redistributes the non–thermal carriers among band states with different spins and momentum directions $\mathbf{k}$. Here we introduce a relaxation time T_1 for the populations $\langle\hat{h}^\dagger_{-\mathbf{k}n}\hat{h}_{-\mathbf{k}n}\rangle$ that determine the hole spin in Eq.(3), which thus reflects the hole spin relaxation time. The latter was calculated in Ref.[50] to be several 10's of fs and was measured in (Ga,Mn)As to be in the range of ∼200fs.[62] Momentum scattering and carrier relaxation is also expected to give T_2 of few 10's of fs.[6,50] Below we estimate the dependence of the predicted non–thermal effects on T_1 and T_2.

The present calculations describe the spin photogeneration that initiates the dynamics. Our main focus is on the average hole spin $\Delta\mathbf{s}_h$(t) coming from e–h photocarriers, whose non–Fermi–Dirac population of band continuum states depends on the laser frequency ω_p. The results presented here were obtained for $\hbar\omega_p\approx$3.1eV.[7,34] For such high frequencies, the disorder–induced impurity/defect states[27] do not contribute significantly and the photoexcited carriers are initally well–separated in energy from the Fermi sea holes (see Fig. 1(a)). We mainly excite band states along the eight {111} symmetry lines of the Brillouin zone, at high $\mathbf{k}$, where the conduction and valence bands are strongly non–parabolic and almost parallel to each other.[7] As a result, a large number of inter–band optical transitions are excited and a broad range of band momenta $\mathbf{k}$ is populated (see Fig. 1(a)). The effects of such highly anisotropic band continua on the photoexcited hole spin are accounted for as described in Appendix B. Due to the symmetry–breaking introduced by $\mathbf{S}$(t), the eight {111} directions not equivalent, unlike in GaAs, which leads to anisotropy. Assuming smoothly varying exchange constant $\beta_{\mathbf{k}}$, the hole spin matrix element $\hat{\mathbf{s}}^h_{\mathbf{k}nn'}$ is fairly constant over a wide range of $\mathbf{k}$, but differs between the eight photoexcited {111} directions. In this case, the contribution to the average spin $\Delta\mathbf{s}_h$(t) from each band n and each direction of $\mathbf{k}$ is approximately proportional to the photoexcited densities $\frac{1}{V}\sum_k \Delta\langle\hat{h}^\dagger_{-\mathbf{k}n}\hat{h}_{-\mathbf{k}n}\rangle$. Our calculation estimates these anisotropic total densities prior to full inter–band relaxation and large momentum scattering between different symmetry directions leading to hole spin relaxation. By tuning the laser frequency ω_p, we create a short–lived imbalance between different bands n, whose spin–admixture differs due to the different spin–orbit interactions. Fermi–Dirac populations of relaxed non–equilibrium holes add to the $\Delta\mathbf{s}_h$(t) calculated here. For $\hbar\omega_p\approx$1.5eV,[35] one excites smaller $\mathbf{k}$ along all {100}, {010}, {001}, {110}, {101}, {011}, and {111} symmetry directions,[66] as well as a distribution of impurity/defect states inside the semiconductor bandgap.[6,27] Despite this difference, the qualitative conclusions of our work apply to all frequencies. The main requirement is to be able to coherently induce a non–equilibrium population imbalance between different bands and momentum directions, which here is facilitated by the symmetry breaking.

Important for bringing the local and mobile spin sub–systems away from equilibrium is the difference in their ultrafast dynamics. Unlike for the band carriers, there is no spin–orbit or optical field coupling of the local spins here. In equilibrium, the local and mobile collective spins are correlated in the ferromagnetic state, so that $\mathbf{S}\times\mathbf{H}_{FS}$=0.[6] Within the mean–field approximation, $\mathbf{S}$(t) is driven out of this equilibrium configuration according to a Landau–Lifshitz–Gilbert equation.[24] The latter describes a magnetization re–orientation driven by both quasi–equilibrium ($\mathbf{H}_{FS}$) and non–thermal ($\Delta\mathbf{s}_h$) mobile carrier spins, which modifies the electronic states:

$$\partial_t\mathbf{S} = -\gamma\mathbf{S}\times\mathbf{H}_{FS}[\mathbf{S}(t)] - \beta\mathbf{S}\times\Delta\mathbf{s}_h(t) + \frac{\alpha}{S}\mathbf{S}\times\partial_t\mathbf{S}, \quad (11)$$

where α characterizes the slow local spin precession damping.[32] Laser–induced magnetization amplitude changes are not captured by this mean–field approximation and require treatment of spin–charge correlations described in Refs.[4,27,39,40]. By including such correlations, longitudinal demagnetization effects triggered by the non–equilibrium population imbalance give a magnetization amplitude S(t), which is distinguished from the transverse effects of main interest here.

The dynamics of the mobile carrier spin depends not only on the magnetic exchange interaction with the local spin but also on spin–orbit coupling, direct nonlinear coupling to the optical field, and fast relaxation:[17]

$$\partial_t\mathbf{s}^h_{\mathbf{k}} = \beta c\mathbf{S}\times\mathbf{s}^h_{\mathbf{k}} + i\langle[H_{so},\mathbf{s}^h_{\mathbf{k}}]\rangle + Im\,\mathbf{h}_{\mathbf{k}}(t) + \partial_t\mathbf{s}^h_{\mathbf{k}}\big|_{rel}. \quad (12)$$

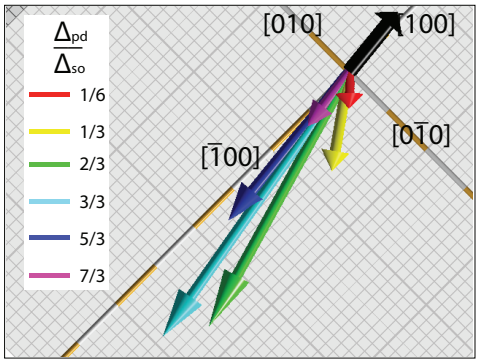

FIG. 2: (Color online) Maximum of anisotropy field $\beta\Delta\mathbf{s}_h$(t) photoexcited by a single 100fs linearly–polarized laser pulse, as function of energy ratio Δ_{pd}/Δ_{so} characterizing time–reversal symmetry breaking. The direction of the ground–state magnetization is along the X^+ easy axis represented by the black arrow close to [100]. $\hbar\omega_p$=3.14eV, E_0=7×10^{5}V/cm, T_1=100fs, T_2=50fs.

The above equation is not useful here, as it does not distinguish between different bands in order to treat the spin–orbit coupling H_{so}. Nevertheless, it demonstrates the four processes that determine the non–thermal carrier spin. The first term describes spin–torque due to magnetic exchange. The second term describes *spin–orbit torque*, obtained here by calculating the density matrix Eq.(5). The third term describes Raman–type coherent nonlinear optical processes that drive photoexcitation of band carrier spin with symmetry–breaking:[17]

$$\mathbf{h}_{\mathbf{k}}(t) = 2\sum_{mn}\langle\hat{h}_{-\mathbf{k}n}\hat{e}_{\mathbf{k}m}\rangle\sum_{m'}\mathbf{d}^*_{\mathbf{k}mm'}(t)\cdot\mathbf{s}^h_{\mathbf{k}m'n}, \quad (13)$$

where $d_{\mathbf{k}mm'}(t) = \mu_{\mathbf{k}mm'}\cdot\mathbf{E}$(t) are the Rabi energies of optical transitions between band states ($m\mathbf{k}$) and ($m'\mathbf{k}$) and $\mathbf{E}$(t) is the laser E–field. Finally, the last term describes the fast spin relaxation due to scattering processes.[17,50]

Spin–orbit and magnetic exchange couplings play an important role during fs photoexcitation: their non–perturbative interplay determines the direction and magnitude of the photoexcited carrier spin. The strong dependence of the maximum of the photoexcited hole fs spin–pulse $\beta\Delta\mathbf{s}_h(t)$ on the energy ratio Δ_{pd}/Δ_{so} is demonstrated by Fig. 2. This result was obtained by solving the coupled equations of motion discussed in Appendix A. Fig. 2 demonstrates a strong dependence of photohole net spin direction and magnitude on Δ_{pd}/Δ_{so}. In the ground state, the magnetization $\mathbf{S}_0$ points along the X^+ easy axis close to [100] (Fig. 2). For $\Delta_{pd}\ll\Delta_{so}$, $\Delta\mathbf{s}_h$ is negligible without circularly–polarized light. The average spin vanishes since all symmetric directions in the Brillouin zone are excited equally. With increasing Δ_{pd}, the magnetic exchange interaction introduces a preferred direction along $\mathbf{S}$(t), which breaks the time–reversal symmetry of GaAs and results in a net $\Delta\mathbf{s}_h$(t) while the laser pulse couples to the magnetic system. With increasing Δ_{pd}/Δ_{so}, the magnitude of this $\Delta\mathbf{s}_h$ increases and its direction changes. For $\Delta_{pd}/\Delta_{so}\sim1/3$, as in (Ga,Mn)As, Fig. 2 shows that the in–plane component of the fs anisotropy field $\beta\Delta\mathbf{s}_h$ points close to the [$\bar{1}\bar{1}$0] direction for $\hbar\omega_p$=3.14eV. As discussed below, this result is consistent with the experimental observations. The above $\Delta\mathbf{s}_h$(t) only lasts during the 100fs laser pulse and drives a "sudden" magnetization canting $\Delta\mathbf{S}$(t) via fs spin–orbit torque. As Δ_{pd} approaches Δ_{so}, $\Delta\mathbf{s}_h$ is maximized while it changes direction. It decreases again for $\Delta_{pd}\gg\Delta_{so}$. In the next section we compare to experiment.

III. EXCITING SPIN DYNAMICS WITH A SINGLE PULSE: THEORY VS EXPERIMENT

Ultrafast magneto–optical experiments in (III,Mn)V semiconductors have revealed magnon oscillations with frequency $\Omega\sim$100ps^{-1}, which can be suppressed (enhanced) with a control laser pulse delayed by τ if $\Omega\tau=\pi$ ($\Omega\tau=2\pi$).[37] In this paper we propose a different optical coherent control scheme, based on controlling the *direction, duration, and magnitude* of fs spin-orbit torque seuqences photoexcited at any time τ. We are not aware of any experiment so far showing laser–induced 360° switchings between multiple magnetic states and suppression of switching rotation at an arbitrary magnetic state. In subsequent sections we explore how to observe our theoretical prediction experimentally by using pulse–shaping. In this section, we validate our original prediction of fs spin–orbit torque in (III,Mn)V materials,[3] by comparing numerical results obtained for anisotropic, non–parabolic band continua with existing experiments showing fs magnetic hysteresis excited by a single 100fs laser pulse in (Ga,Mn)As. It is certainly valuable to establish the connection of our theory with this experiment before making numerical predictions of complex protocols based on trains of laser pulses with various timing sequences and colors. As discussed in subsequent sections, laser–pulse–trains provide a more controlled way to enable multiple switchings by manipulating fs spin–orbit torques. In this way we maximize "transverse" hole spin excitations while keeping the pump fluence as low as possible (10–100 μJ/cm^2) to reduce the "longitudinal" fs demagnetization. The direct theory–experiment comparison in this section, as well as the indirect connection to other experiments[35] discussed later, makes the case that optical control of a short–lived coherent population imbalance between exchange–split, spin–orbit–coupled anisotropic bands can generate fs spin–orbit torque with controllable direction, temporal profile, and magnitude.

Fig.3 shows the detailed fs temporal profile of the pump–probe magneto–optical signal of our (Ga,Mn)As sample as function of perpendicular magnetic field. Unlike previous experiments that measured magnetization dynamics on the ps timescale, Fig.3 shows the initial ∼100fs temporal regime. As we demonstrate below, this regime reveals a sizable carrier–spin pulse with ∼100fs

duration, which generates a transverse magnetization component that cannot arise from longitudinal nonlinear optical or demagnetization effects. The details of the experimental methods and (Ga,Mn)As sample may be found in Ref.[34]. The 100fs pump pulse, with central frequency $\hbar\omega_p$=3.1eV, is well–separated in energy from the probe tuned at 1.55eV, which minimizes pump–probe interference. The pump optical field, with amplitude $E_0 \sim 2\times10^5$V/cm and fluence $\sim 7\mu$J/cm^2, excites a total photohole density of $n \sim 6\times10^{18}$/cm^3. This is a small perturbation of the 3×10^{20}/cm^3 ground state hole density in our (Ga,Mn)As sample. $\Delta S_z/S \propto \Delta\theta_K/\theta_K$ is probed via the pump–induced Kerr rotation angle $\Delta\theta_K$ along the [001] direction.[8] The magnetic origin of the measured signal is implied by two experimental observations. First, $\Delta\theta_K$ coincides with the pump–induced ellipticity even during $\sim$100fs.[34] Second, we observe a systematic B–field dependence and sign switching of $\Delta\theta_K$, absent in θ_K without pump, which directly correlates with the magnetic switchings observed in the static transverse Hall magnetoresistivity.[34] We measure a transverse fs magnetization component ΔS_z(t), perpendicular to the ground state magnetization, which switches direction with initial magnetic state. This transverse component is suppressed by increasing the magnetic field perpendicular to the sample plane and easy axes. The observed "sudden" step–like temporal profile indicates that spin re–orientation completes during the laser pulse and thus is driven by e–h photoexcitation. Such fs time–dependence is clearly distinguished from subsequent "slow" magnon oscillations during $\sim$100ps times.[62]

To elucidate the magnetic origin of the measured $\Delta\theta_K/\theta_K$ with $\sim$100fs duration, we apply a transverse external magnetic field B as in Fig.3(a). For B=0, the magnetic states $X_0^\pm$ and $Y_0^\pm$ lie inside the plane (Fig. 1(b)). For $B\neq0$, Eq.(A11) gives an out–of–plane canting of $X^\pm$ and $Y^\pm$ (Fig. 3(a)). In the absence of pump, the measured smooth change of static Kerr rotation angle θ_K as function of B–field, discussed in Refs.[34,62], reflects this canting. There is no magnetic hysteresis of $\theta_K(B)$ without the pump. This is unlike the behavior demonstrated by Fig. 3, which shows the changes in the fs temporal profile of $\Delta\theta_K/\theta_K$ induced by sweeping the magnetic field between B=$-1T$ and B=$1T$. By comparing the fs response between increasing ("up") and decreasing ("down") B–field,[34] we observe in Figs. 3(b) through (f) a magnetic hysteresis of the laser–induced fs change $\Delta\theta_K/\theta_K$. This magnetic hysteresis and sign switchings coincide with the magnetic hysteresis measured in the static Hall magnetoresistivity.[34] This coincidence implies that $\Delta\theta_K/\theta_K$ (or the identical pump–induced ellipticity) reflects fs dynamics of $\Delta S_z/S$, whose sign correlates with the switchings of equilibrium magnetization induced by transverse B–field as discussed next.

S_z varies smoothly with increasing or decreasing B–field (Eq. A11), consistent with the observed smooth variation of $\theta_K(B)$.[34] In contrast, when the sweeping of B–field switches the magnetization between $X^\pm$ and $Y^\pm$

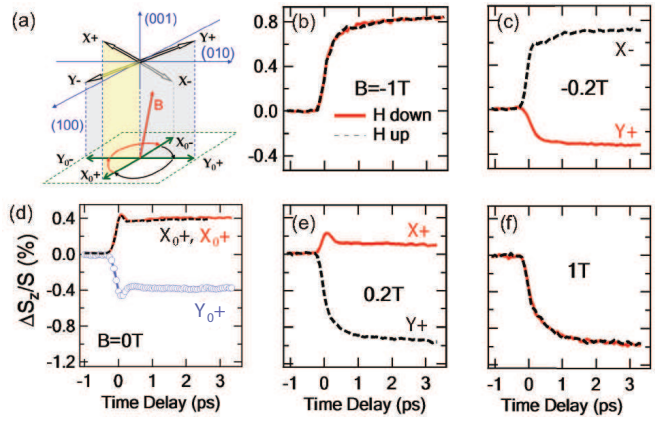

FIG. 3: (Color online) Magneto–optical pump–probe experimental measurements showing a step–like, laser–induced, fs magnetization canting ΔS_z(t) that displays a fs magnetic hysteresis and switches direction when switching magnetic state. (a) An external perpendicular B–field, applied at small angle $\sim 5^o$ from the [001] axis, tilts the B=0 in–plane easy axes ($X_0^\pm$ and $Y_0^\pm$) out of the plane (Appendix A). (b)–(f): The "sudden" out–of–plane magnetization $\Delta S_z/S$, induced by a 100fs laser pulse with fluence $\sim 7\mu J/cm^2$, switches direction when sweeping the above B–field between B=-1T (b) and B=1T (f). The two sweeping directions correspond to increasing (up, full curves) and decreasing (down, dashed curves) B–field. For each of the measured B=1T, 0.2 T, 0 T, -0.2T, -1T, the fs temporal profiles of $\Delta S_z/S$ depend on the equilibrium magnetic state, which is switched when sweeping the B–field.

equilibrium states, as seen in the static Hall magnetoresistivity, the direction of pump–induced fs component ΔS_z also switches sign. As discussed below, this behavior is consistent with our theory. The observed dependence of the sign of fs $\Delta\theta_K$ on the equilibrium easy axis cannot be explained by invoking conventional nonlinear optical effects or magnetization amplitude "longitudinal" changes.[8,26–28] When the latter dominate, X^+ (X^-) give the *same* ΔS_z as Y^+ (Y^-). Indeed, here the two in–plane easy axes and, thereby, the in–plane magnetic states are equivalent (symmetric) with respect to the probe propagation direction, which is perpendicular to the X–Y plane. However, Fig.3(d) (B=0) and Figs.3(c) and (e) (B=$\pm0.2T$) clearly show that this is not the case. This is in sharp contrast to large B=$\pm$1T: Figs. 3(b) and (f) show the same exact fs changes for both increasing or decreasing B, which thus do not depend on easy axis. As we discuss below, fs magnetization re–orientation due to fs spin–orbit torque diminishes with increasing perpendicular B, consistent with the above behavior.

For B=0, Fig.3(d) reveals a *symmetric and opposite* out–of–plane fs canting ΔS_z(t) between the X_0 and Y_0 initial states. In this case, the initial magnetization $\mathbf{S}_0$ lies inside the sample plane and $S_z\approx0$ in equilibrium (Fig. 3(a)). Thus, the observed ΔS_z(t) cannot be associated with an amplitude change, as it occurs in a direction [001] perpendicular to $\mathbf{S}_0$. For large B, the

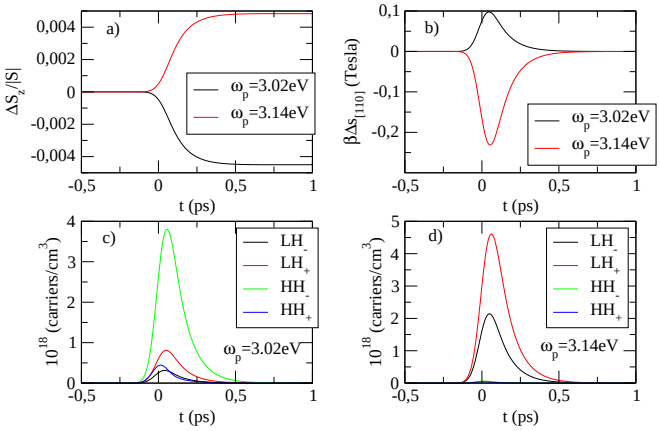

FIG. 4: (Color online) Frequency dependence of local and mobile spin dynamics and photohole populations following excitation by a 100fs linearly–polarized laser pulse with low pump fluence $\sim 10\mu J/cm^2$. The initial magnetization points along the X^+ easy axis. (a): Comparison of "sudden" out–of–plane magnetization for $\hbar\omega_p$=3.14eV (LH optical transitions) and $\hbar\omega_p$=3.02eV (HH optical transitions). (b): Comparison of non–adiabatic photoexcited hole spin component along [110] for the two above frequencies. (c): Coherent photoexcited hole populations of the four different exchange–split HH and LH bands for $\hbar\omega_p$=3.14eV. (d): Same as (c) for $\hbar\omega_p$=3.02eV.

magnetization aligns with the B–field along [001], $S_z \approx S$, and ΔS_z(t) reflects longitudinal fs changes in magnetization amplitude.[27,40] For B=0, $S_z \approx 0$ and ΔS_z(t) reflects transverse changes in magnetization direction. The opposite sign of laser–induced femtosecond ΔS_z(t) between the $X_0^{\pm}$ and $Y_0^{\pm}$ states, Fig.3(d), can only arise from fs magnetization rotation towards opposite out–of–plane directions. Furthermore, except for the sign difference, the fs temporal profiles of $\Delta S_z/S$ in Fig.3(d) are *symmetric* between X_0 and Y_0. This symmetry implies that the out–of–plane ΔS_z is driven by a laser–induced anisotropy field pulse that points close to the diagonal direction between X_0 and Y_0. The step–like temporal profile implies that this field has $\sim$100fs duration. The above experimental observations are consistent with the direction and duration of $\Delta \mathbf{s}_h$ calculated in Fig. 2 for anisotropy parameter $\Delta_{pd}/\Delta_{so} \sim 1/3$ similar to (Ga,Mn)As. Such calculated spin–pulse, discussed further below, exerts a fs spin–torque $\propto \Delta \mathbf{s}_h \times \mathbf{S}_0$, whose out–of–plane direction changes sign while its magnitude remains the same for $\mathbf{S}_0$ along X_0 or Y_0. Note that laser–induced thermal effects due to spin–lattice coupling can change the equilibrium easy axis,[32,35] but such changes occur gradually in time over many ps. In contrast, here we observe step–like magnetization changes that follow the 100fs laser pulse and are consistent with the predicted fs spin–orbit torque.

To relate our calculations to Fig.3, we first take B=0 and show in Fig. 4 the spin and charge dynamics for a single linearly–polarized 100fs laser pulse, with E_0=2×10^{5}V/cm similar to the experiment. The initial state is X_0^+. We compare the spin and charge population dynamics for two different laser frequencies, $\hbar\omega_p$=3.14eV and $\hbar\omega_p$=3.02eV, tuned to excite different band continua around 3.1eV. In Fig. 4(a) we show the development in time of the optically–induced out–of–plane local spin component ΔS_z(t). The calculated step–like fs temporal profile agrees with Fig. 3. Furthermore, we observe a reversal in the direction of ΔS_z when tuning the photoexcitation frequency. The fs spin–orbit torque leading to such ΔS_z(t) is exerted by the photohole spin–pulse $\Delta \mathbf{s}_h$(t), whose component along the diagonal [110] direction is shown in Fig. 4(b) for the two above frequencies. The magnitude, direction, and temporal profile of both local and mobile spin components in Figs. 4(a) and (b) are consistent with the experimental results of Fig. 3(d).

Important for controlling the four–state magnetic memory is that we are able to reverse the direction of the out–of–plane magnetization tilt ΔS_z, Fig.4(a), and photoexcited hole spin–pulse, Fig.4(b), by exciting e–HH ($\hbar\omega_p$=3.02eV) or e–LH ($\hbar\omega_p$=3.14eV) optical transitions. The origin of this spin–reversal can be seen by comparing the total populations $\frac{1}{V}\sum_{\mathbf{k}} \Delta\langle \hat{h}^{\dagger}_{-\mathbf{k}n} \hat{h}_{-\mathbf{k}n}\rangle$ for the four different exchange–split HH and LH valence bands n in all {111} $\mathbf{k}$–directions These band–resolved spin–polarized total populations are shown in Figs. 4(c) and (d) as function of time for T_1=100fs, which is comparable to the measured[62] and calculated[50] hole spin relaxation time. More than one bands are populated simultaneously due to the energy dispersion and laser–pulse–width. With frequency tuning we create a controlled short–lived imbalance between exchange–split bands with different spin–orbit couplings and spin admixtures. In this way we coherently control the superposition of spin–↑ and spin–↓ states prior to spin relaxation, here during the 100fs pulse. The order of magnitude of the photocarrier densities, calculated by including the band continua along all eight {111} $\mathbf{k}$–directions and using the GaAs tight–binding parameters of Ref.[51] (Appendix B), agrees with the experimentally–measured densities $n \sim 6\times 10^{18}$/cm^3 for the same pump fluence. For such photohole populations, we also obtain $\Delta S_z/S$ with same order of magnitude and direction as in the experiment (compare Figs. 4(a) and 3(d)). The calculated $\sim$250mT component of $\beta\Delta \mathbf{s}_h$(t) along [110], Fig. 4(b), agrees with the 100fs magnetic anisotropy field extracted from Fig. 3(d) and is larger than typical fields obtained from calculations that assume a non–equilibrium Fermi–Dirac distribution.[35] This theory–experiment agreement indicates that non–thermal populations with lifetimes T_1=100fs comparable to the hole spin lifetimes in (Ga,Mn)As[50,62] can explain the observed impulsive ΔS_z(t).

Further evidence in favor of the proposed fs spin–orbit torque mechanism is obtained from the pump–induced fs magnetic hysteresis observed in the experiment of Fig. 3. In Fig. 5(a) we compare the fs canting ΔS_z/S, calculated at t=500fs as function of B along [001], for the four B–dependent magnetic states $X^{\pm}$ and $Y^{\pm}$. Fig. 5(a) shows that switching between X and Y states, induced in the

experiment by sweeping B, switches the sign of ΔS_z(t) (fs magnetic hysteresis). Furthermore, Fig. 5(a) shows that fs magnetization re–orientation diminishes with increasing B and practically vanishes at high magnetic fields. The above results, consistent with Fig. 3, explain the observed coincidence of ΔS_z switchings with static planar Hall effect switchings[34] and the absence of hysteresis at high B. While nonlinear effects such as dichroic bleaching contribute to the fs magneto–optical signal, the observed systematic B–field dependence and magnetic hysteresis in the sign of $\Delta\theta_K/\theta_K$ indicate non–adiabatic origin consistent with our calculations of fs spin–orbit torque.

For high B–fields, only longitudinal changes in magnetization amplitude[28] and nonlinear optical effects contribute to Fig. 3(b) and Fig. 3(f). The mean–field density matrix factorization used here does not capture magnetization amplitude changes, which appear at the level of electron–magnon spatial correlations.[39,40] As discussed in Ref.[27], any photoinduced imbalance of spin–↑ and spin–↓ states will lead to fs demagnetization and inverse Overhauser effect, which is independent of easy axis direction. While such imbalance may arise from photoinduced changes in the Fermi–Dirac temperature and chemical potential, a large electronic temperature increase is required to produce the broad distributions implied by the magnitude of the experimentally–observed effects.[27] The broad non–thermal populations considered here create an imbalance that, for $T_1 \leq$100fs, follows the laser pulse. In contrast, relaxation to the lattice bath is slower (ps).[27] Both "longitudinal" and "transverse" fs spin dynamics arise from the competition of spin–orbit and magnetic–exchange interactions, but manifest themselves differently for different photoexcitation conditions and external magnetic fields. Femtosecond demagnetization (decrease in Mn spin amplitude) through dynamical polarization of longitudinal hole spins dominates for high fluences of 100s of μJ/cm^2.[62] Our proposed pulse–train scheme achieves spin rotational switching by using lower pump intensities that reduce fs demagnetization.

As already seen in Fig. 4, by coherently controlling the non–thermal population imbalance between the four exchange–split HH and LH bands, we can control the direction of out–of–plane ΔS_z/S. This is seen more clearly in Fig. 5(b), which shows the frequency–dependence of ΔS_z/S and compares it to the individual contributions obtained by retaining one valence band at a time. The non–equilibrium population of band states with different spin admixtures leads to different directions of laser–induced ΔS_z(t). For example, photoholes excited in the two exchange–split (HH or LH) valence bands induce opposite out–of–plane tilts. The finite pulse–duration and strong band dispersion and non–parabolicity (Appendix B and Fig. 1(a)) lead to different populations of more than one bands at all frequencies. We conclude that optical control of the photoexcited carrier populations can be used to switch the directions of photoexcited fs spin–orbit torques and, in this way, control the direction of fs magnetization tilts.

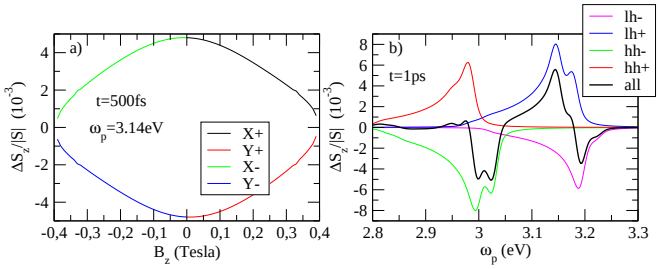

FIG. 5: (Color online) The fs magnetic hysteresis and frequency dependence of photoinduced magnetization canting $\Delta S_z/S$ characterize the proposed fs spin–orbit torque non–adiabatic mechanism. (a): The direction of out–of–plane fs component $\Delta S_z/S$ depends on the easy axis (magnetic hysteresis) and magnetic field direction. This magnetic hysteresis diminishes with increasing perpendicular B–field due to suppression of laser–induced magnetization re–orientation, which separates experimentally "transverse" and "longitudinal" spin dynamics. (b): Frequency dependence of laser–induced $\Delta S_z/S$ and its individual contributions from the four exchange–split HH and LH bands, calculated at t=1ps for E_0=2×10^{5}V/cm. Initial magnetization points along X^+. The band continua significantly affect the frequency dependence of ΔS_z(t) as compared to discrete–**k** special point calculations.

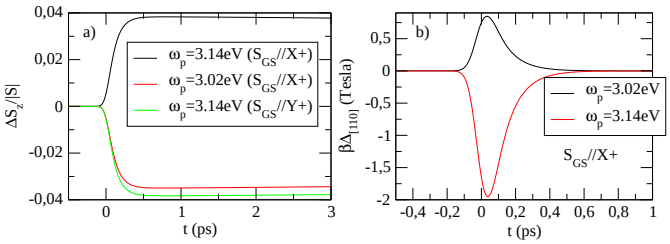

FIG. 6: (Color online) Calculated fs spin dynamics similar to Fig. 4 but with order of magnitude higher pump fluence $\sim$100$\mu J/cm^2$. (a) Comparison of out–of–plane magnetization components for two different initial magnetic states and ω_p. (b) Photohole fs anisotropy fields along [110] for the two ω_p.

The precise magnitude of the proposed effects depends on the relaxation timescales. The non–thermal populations are created during the 100fs laser pulse, via e–h optical polarization, with dephasing time T_2, driven by the laser field. They relax on a timescale T_1 that is comparable to hole spin relaxation.[50,62] The above characteristic times are expected to be in the 10-200fs range.[50,62] For pump fluences of $\sim$10$\mu J/cm^2$, the experiment gives $\Delta S_z/S\sim$0.5%, which we reproduced for T_1=100fs and T_2=50fs. This contribution decreases to $\Delta S_z/S\sim$0.01% as T_2 decreases to 3fs with fixed T_1=100fs. For fixed short T_2=10fs, $\Delta S_z/S$ varies between $\sim$0.05-0.1% as T_1 varies between 30fs and 100fs. We conclude that the fs spin–orbit torque contribution has the same order of magnitude as the experimental result unless both T_1 and T_2 are only few fs. From now on we fix T_1=100fs and T_2=50fs.

The non–thermal/non–adiabatic fs spin–orbit torque contribution can be enhanced by increasing the laser intensity. Fig. 6(a) shows that, for easily attainable $\sim 100\mu J/cm^2$ pump fluences,[35] the "sudden" magnetization tilt increases to $\Delta S_z/S \sim 4\%$ (for $E_0 = 7\times 10^5$V/cm), while Fig. 6(b) shows that $\beta\Delta\mathbf{s}_h$(t) along [110] then grows into the Tesla range. The precise value is sample–dependent and depends on the relaxation. While the quasi–equilibrium contribution $\mathbf{H}_{FS}$ is limited by the chemical potential, $\beta\Delta\mathbf{s}_h$ is controlled by the laser frequency. The different intensity–dependence and temporal profiles of thermal and coherent/non–thermal carrier spin components can separate these two contributions. A distinct impulsive component of fast magnetic anisotropy was observed in the ps magnetization trajectory measured in Ref.[35] for pump fluences above $\sim 70\mu J/cm^2$ and $\hbar\omega_p \sim 1.5$eV. Finally, Fig. 6(a) compares the dynamics for initial magnetization along the X_0^+ or Y_0^+ easy axis for B=0. Similar to the experiment of Fig. 3(d), it displays symmetric temporal profiles of ΔS_z(t), with opposite signs for the two perpendicular easy axes. In this way, we can distinguish the magnetic states within 100fs. The equal magnitude of ΔS_z between the two perpendicular in–plane easy axes arises from the diagonal direction of $\Delta\mathbf{s}_h$ obtained for $\Delta_{pd}/\Delta_{so} \sim 1/3$ as in (Ga,Mn)As (Fig. 2). The overall agreement between theory and experiment suggest that a magnetic state can be read within 100fs, by monitoring the direction of out–of–plane laser–induced magnetization canting. In the next section we discuss how one could also switch the four–state magnetic memory with low intensity by using pulse–shaping.

IV. INITIATING DETERMINISTIC SWITCHINGS WITH A LASER–PULSE–TRAIN

A single 100fs laser pulse with $\sim$10–100μJ/cm^2 fluence excites magnon oscillations around the equilibrium easy axis. Laser–induced switching of the magnetization to a different magnetic state requires photoexcitation of a stronger "initial condition" $\Delta\mathbf{S}$(t). While switching may be possible by increasing the pump intensity,[36] pulse–shaping[22] can be used to initiate it in a more controlled way while keeping the laser fluence per pulse as low as possible to reduce fs electronic heating of spins. We coherently control $\Delta\mathbf{s}_h$(t) with M time–delayed trains of N Gaussian τ_p=100fs laser pulses:

$$\mathbf{E}(t) = \sum_{j=1}^{M} \mathbf{E}_0 \sum_{i=1}^{N} \exp[-(t-\tau_j-\Delta\tau_{ij})^2/\tau_p^2] \times \exp[-i\omega_p^{(j)}(t-\tau_j-\Delta\tau_{ij})]. \quad (14)$$

We tune τ_j, the time delay of the j-th laser–pulse–train, and $\omega_p^{(j)}$, the pulse–train central frequency but fix $\Delta\tau_{ij}$=500fs for simplicity. In this section we consider M=1 and control the net duration of successive fs spin–orbit torques by using a train of N pulses. In Fig. 7 we compare the components of $\beta\Delta\mathbf{s}_h$(t) and $\gamma\Delta\mathbf{H}_{FS}$ in the coordinate system defined by the [110], [1-10], and [001] directions. We use the same $\sim 100\mu$J/cm^2 fluence as in Fig. 6, but increase the number of pulses from N=1 to N=8. The non–thermal contribution $\beta\Delta\mathbf{s}_h$(t) now prevails, while $\Delta\mathbf{H}_{FS}$(t) builds–up as $\Delta\mathbf{s}_h$ drives $\Delta\mathbf{S}$(t) and forces the spin of the Fermi sea bath to adjust to the new direction of $\mathbf{S}$(t).[17] $\Delta\mathbf{S}$(t) builds–up in a step–by–step fashion well before relaxation, driven by photoexcited sequences of successive fs spin–orbit torques.

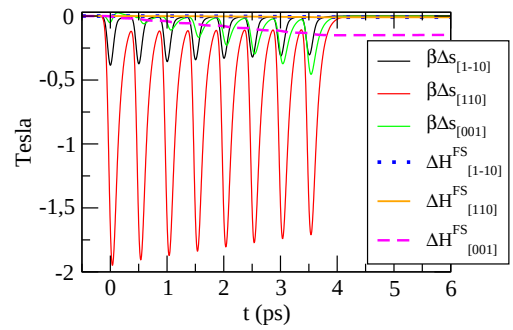

FIG. 7: (Color online) Comparison of non–thermal and quasi–thermal components of laser–induced magnetic anisotropy fields $\beta\Delta\mathbf{s}_h$(t) and $\Delta\mathbf{H}_{FS}$(t) during coherent nonlinear photoexcitation with a train of N=8 100fs laser pulses separated by 500fs, with $E_0 = 7\times 10^5$V/cm and $\hbar\omega_p$=3.14eV.

$\Delta\mathbf{H}_{FS}$(t) originates from the spin of the thermal hole Fermi sea and is therefore restricted by the Fermi–Dirac distribution. Such populations give anisotropy fields of the order of few 10's of mT in (Ga,Mn)As,[6,35] restricted by the $\sim\mu$eV free energy differences close to the Fermi level. On the other hand, the experiments observe anisotropy fields that are at least one order of magnitude higher.[34,35] Fig. 7 shows $\beta\Delta\mathbf{s}_h$(t) calculated in the time–domain, by solving density matrix equations of motion after taking into account the (Ga,Mn)As bandstructure. It comes from the short–lived non–thermal populations photoexcited at $\hbar\omega_p$=3.14eV. These populations are not restricted by the Fermi–Dirac distribution and access parts of the Brillouin zone that are empty close to quasi–equilibrium. $\beta\Delta\mathbf{s}_h$(t) can grow to $\sim$2T along [110] for experimentally–relevant pump fluences and photocarrier thermalization times $T_1 \sim 100$fs. For such fast relaxation, $\Delta\mathbf{s}_h$(t) follows the laser–pulse–train temporal profile and the relative phase of consequative pulses does not play a role. However, $\Delta\mathbf{s}_h$(t) is not the same for different pulses, as the non–equilibrium electronic states change non–adiabatically with $\Delta\mathbf{S}$(t) (Appendix A).

We now show that, by tuning N, we can initiate switching rotation to any one of the available magnetic states, instead of exciting magnon oscillations around the equilibrium easy axis. Fig. 8 shows three magnetization switching trajectories up to long times t=800ps. These ps trajectories are initiated at t=0 by N=7 (Fig. 8(a)), N=9 (Fig. 8(b)), or N=12 (Fig. 8(c)) laser pulses with

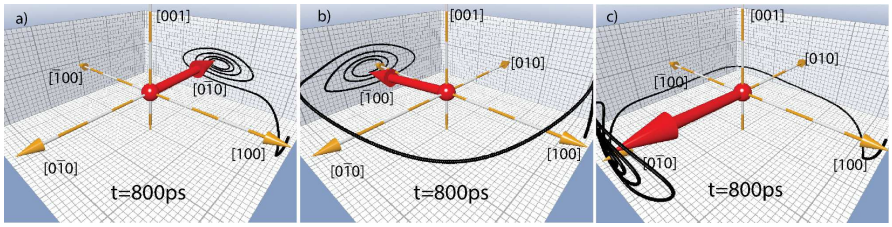

FIG. 8: (Color online) Magnetization switching trajectories from X^+ to the other three magnetic states, triggered by trains with increasing number of laser pulses N and E_0=7×10^{5}V/cm. All switchings are followed by pronounced magnetic ringing. (a): Counter–clockwise 90° switching $X^+ \rightarrow Y^+$, initiated by HH photoexcitation with N=7 pulses. (b): 180° magnetization reversal via clockwise pathway $X^+ \rightarrow Y^- \rightarrow X^-$, initiated by LH photoexcitation with N=9 pulses. (c): Photoexcitation as in (a), but with N=12 pulses. By increasing N we can move the magnetization past the Y^+ and X^- intermediate states and access the Y^- state via the 270° counter–clockwise pathway $X^+ \rightarrow Y^+ \rightarrow X^- \rightarrow Y^-$.

∼100μJ/cm^2 fluence. By increasing N, we switch from X^+ to all three of the other magnetic states Y^+, X^-, and Y^-. In Fig. 8(a), N=7 pulses with $\hbar\omega_p$=3.02eV (HH photoexcitation) initiate a counter–clockwise 90° switching rotation that stops after reaching the next magnetic state, Y^+, within ∼80ps. The magnetization oscillates around the final state with a significant amplitude that cannot be controlled with a single pulse–train (magnetic ringing).[46] This ringing results from the weak (nanosecond) Gilbert damping of the local–spin precession observed in annealed (Ga,Mn)As.[32,35] While magnetic ringing can make the multiple 90° switchings unstable, below we show that we can suppress it by exerting opposing fs spin–orbit torques. By increasing the number of pulses to N=9, the magnetization continues past Y^+ to the next available state, X^-. Fig. 8(b) shows a magnetization reversal via clockwise instead of counter–clockwise rotation, since $\hbar\omega_p$=3.14eV excites e–LH instead of e–HH optical transitions. This $X^+ \rightarrow Y^- \rightarrow X^-$ pathway completes within ∼150ps in (Ga,Mn)As and is again followed by magnetic ringing. By increasing the number of pulses further, to N=12, the initial fs spin–orbit torque is sufficient to move the magnetization even beyond X^-. Fig. 8(c) shows 270° switching to the Y^- state within ∼200ps, following the $X^+ \rightarrow Y^+ \rightarrow X^- \rightarrow Y^-$ pathway initiated by e–HH photoexcitation.

V. OPTICAL CONTROL OF SEQUENTIAL 90° SWITCHINGS BETWEEN FOUR STATES

In this section we study the possibility to manipulate fs spin–orbit torques in order to gain full ultrafast access of this four–state magnetic memory. Fig. 9 shows two switching protocols that achieve 360° control of the magnetic states of Fig. 1(b). The upper panel shows the sequences of laser–pulse–trains used to control the four sequential 90° switchings. Two different laser frequencies excite e–HH or e–LH optical transitions that stop and restart the magnetization motion at each of the four magnetic states. By tuning the laser frequency, we choose the direction of this multi–step switching process, which takes place via counter–clockwise (Fig.9(a)) or clockwise (Fig.9(b)) magnetization rotations forced to stop at all intermediate states. To control the photoexcited $\Delta\mathbf{s}_h$(t) and fs spin–orbit torques, we turn three experimentally accessible "knobs": (i) *Pulse–shaping*[22] by changing N, which controls the net duration and temporal profile of the spin–orbit torques. In this way, we tailor $\Delta\mathbf{S}$(t) that initiates or modifies the switching rotations with low intensity per laser pulse. (ii) *Frequency–tuning* enables selective photoexcitation of exchange–split LH or HH non–equilibrium populations with different superpositions of spin–↑ and spin–↓ states. In this way we control the population imbalance that decides the directions of $\Delta\mathbf{s}_h$, fs spin–orbit torque, and $\Delta\mathbf{S}$(t). (iii) By controlling the *time–delays* τ_j, one can exert fs spin–orbit torques at desirable times in order to stop and restart the switching rotation at all intermediate states and suppress magnetic ringing. This is discussed further in the next section. To understand the role of the twelve laser–pulse–trains in Fig. 9, we note the following points: (i) a laser–pulse–train initiates switchings or magnon oscillations via fs spin–orbit torque with direction that depends on *both* laser frequency and magnetic state, (ii) when the magnetization reaches a new magnetic state, we use a laser–pulse–train to exert opposing fs spin–orbit–torques, in a direction that stops the switching rotation and suppresses the magnetic ringing so that we can access the state, and (iii) when we are ready to move on, a laser–pulse–train with the appropriate color restarts the 360° switching process by exerting fs spin–orbit torques in the desirable direction.

Fig. 9 shows four sequential 90° switchings controlled by $\Delta\mathbf{s}_h$(t). In Fig. 9(a), a counter–clockwise $X^+ \rightarrow Y^-$ switching is initiated by e–HH photoexcitations with N=12 pulses. After τ=35ps, the magnetization reaches the vicinity of the intermediate Y^+ state. We then stop the switching process by exciting e–HH optical transitions. We restart the motion at τ=85ps, after waiting for about 50ps, by using e–LH photoexcitations to switch the magnetization to the X^- state. There we again stop the process at τ=160ps, by exciting e–LH optical transitions. We restart at τ=170ps with e–HH photoexcitations, which trigger switching to Y^-. This

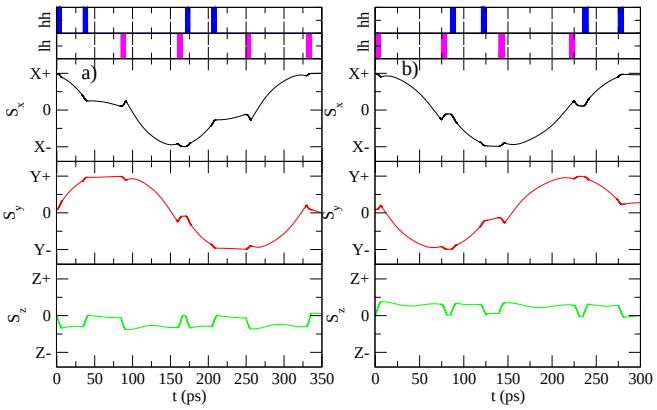

FIG. 9: (Color online) Two protocols for 360° control of the full four–state magnetic memory via four sequential 90° switchings that stop and restart at each intermediate magnetic state. (a) Counter–clockwise sequence $X^+ \rightarrow Y^+ \rightarrow X^- \rightarrow Y^- \rightarrow X^+$, (b) Clockwise sequence $X^+ \rightarrow Y^- \rightarrow X^- \rightarrow Y^+ \rightarrow X^+$. Upper panel: Laser–pulse–train (N=12) timing sequences and colors. Blue pulses excite HH optical transitions, magenta pulses excite LH transitions. E_0=7×10^5V/cm corresponds to pump fluence ≈100$\mu J/cm^2$.

switching completes within ∼35ps, after we stop the motion with e–HH photoexcitations at τ=205ps. We finish the 360° switching loop by using e–LH photoexcitations to restart the counter-clockwise motion back to X^+, at τ=250ps, and later to terminate the process at τ=330ps. Fig.9(b) shows an opposite clockwise switching sequence $X^+ \rightarrow Y^- \rightarrow X^- \rightarrow Y^+ \rightarrow X^+$, obtained by changing the laser–pulse frequencies from e–HH to e–LH excitations and vice–versa. In this case, e–LH optical transitions with N=12 pulses trigger clockwise magnetization rotation, which we suppress at Y^- with LH excitations at τ=75ps. We restart the process with e–HH photoexcitation at τ=85ps and suppress it again at X^- with e–HH optical transitions at τ=120ps. We restart with e–LH excitation at τ=140ps and switch to Y^+, where we suppress the motion at τ=225ps with e–LH optical transitions. We complete a closed switching loop to the initial X^+ state with e–HH photoexcitation at τ=235ps and suppress the rotation with e–HH optical transitions at τ=275ps. In the next section we analyze how tunable fs spin–orbit torque direction offers more flexibility for controlling switching rotations and magnetic ringing.

VI. CONTROLLING MAGNETIC SWITCHING AND RINGING WITH A LASER–PULSE–TRAIN

A multi–state memory allows for more elaborate tests of optical control schemes as compared to simply flipping the spin between two states. In order to selectively access four different magnetic states via 360° magnetization rotation, we must be able to not only initiate switchings, as in Fig. 8, but also to suppress the magnetization motion at any intermediate state. We must also be able to suppress the ringing due to magnetization oscillations around an easy axis. Magnetic ringing arises from the weak damping of the magnetization precession following excitation with either optical or magnetic field pulses and limits the read/write times in many magnetic materials.[46] One known way to reduce it is to take advantage of the phase $\Omega\tau$ of magnetization precession with frequency Ω.[37,46] With magnetic field pulses, this can be done by adjusting the duration of the long pulse to the precession period.[46] With ultrashort laser pulses, one can suppress (enhance) the precession by exciting when $\Omega\tau$=π ($\Omega\tau$=2π), in the same way as at τ=0.[37] Such coherent control of spin precession is possible for harmonic oscillations. Below we show that we can optically control both magnon oscillations and nonlinear switching rotations, at all time delays, by applying either clockwise or counter–clockwise fs spin–orbit torques as needed.

We start with the harmonic limit and demonstrate magnon control via fs spin–orbit torque with tunable direction. First we excite at τ=0 magnon oscillations with frequency Ω (thick solid line in Fig. 10). We thus initiate magnetization precession around the X^+ (Fig. 10(a)) or the Y^+ (Fig. 10(b)) easy axis with e–LH excitation ($\hbar\omega_p$=3.14eV). An impulsive magnetization at τ=0 is observed in the ps trajectory of Fig. 10. The initial phase of these magnon oscillations is opposite between the X_0^+ and Y_0^+ states, due to the opposite directions of the fs spin–orbit torques (Fig. 6(a)). We then send a control laser pulse at τ=74ps ($\Omega\tau$=π) or at τ=148ps ($\Omega\tau$=2π), but use either $\hbar\omega_p$=3.14eV (e–LH optical transitions) or $\hbar\omega_p$=3.02eV (e–HH optical transitions). By controlling the direction of fs spin–orbit torque with such frequency tuning, we show that we can both enhance and suppress the amplitude of the magnetization precession at *both* $\Omega\tau$=π and $\Omega\tau$=2π. While for $\Omega\tau$=π we suppress magnetic ringing when applying the same fs spin–orbit torque as for τ=0 ($\hbar\omega_p$=3.14eV), we enhance it by applying an opposite fs spin–orbit torque ($\hbar\omega_p$=3.02eV). Similarly, at time $\Omega\tau$=2π, we enhance the ringing when applying fs spin–orbit torque in the same direction as for τ=0 and suppress it by reversing the direction. We thus gain flexibility for controlling magnon oscillations.

Unlike for harmonic precession, switching also involves nonlinearities and anharmonic effects. In Fig. 11(a), a $X^+ \rightarrow Y^+ \rightarrow X^- \rightarrow Y^-$ switching pathway (dashed line) is initiated at τ=0 as in Fig. 8(c). After about 200ps, the magnetization switches to Y^-, after overcoming the intermediate states Y^+ and X^-. The X–component of the magnetization then oscillates with a significant amplitude (magnetic ringing, dashed curve in Fig. 11(a) and Fig. 8(c)). Fig. 11(a) (solid curve) demonstrates suppression of this ringing by a control laser–pulse–train that arrives at any time after the switching is completed. To accomplish this, we tune the direction and strength of fs spin–orbit torques. Figs. 11(b) and (c) demonstrate that the control pulse–train can also stop the $X^+ \rightarrow Y^+ \rightarrow X^- \rightarrow Y^-$ switching at one of the intermedi-

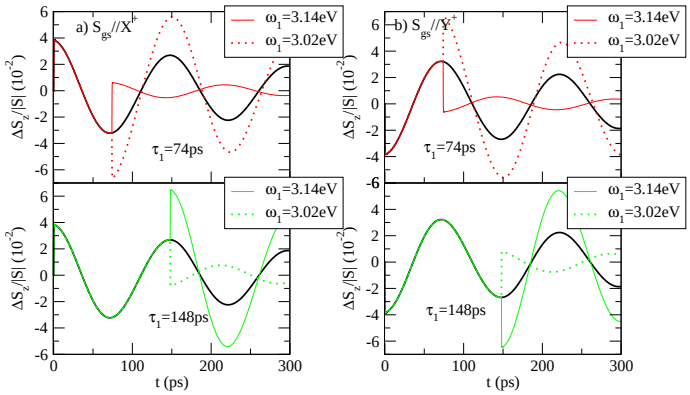

FIG. 10: (Color Online) Two 100fs laser pulses, delayed by τ, control magnon oscillations via fs spin–orbit torque. The first pulse, $\hbar\omega_p$=3.14eV, starts the precession (frequency Ω) at τ=0. The second pulse, $\hbar\omega_p$ = 3.02eV or $\hbar\omega_p$ = 3.14eV, arrives at τ=74ps ($\Omega\tau=\pi$) or τ=148ps ($\Omega\tau=2\pi$). Equilibrium magnetic state: (a): X^+ and (b): Y^+.

ate magnetic states before reaching Y^-. However, we must use different ω_p at Y^+ and X^- in order to get an opposing fs spin–orbit torque, as the direction of the latter depends on the magnetic state. In Fig. 11(b) we stop the switching at the X^- magnetic state, after passing through Y$^+$, by exciting with $\hbar\omega_p$=3.14eV at $\tau\sim$100ps (e–LH photoexcitation). Fig. 11(c) shows that we can stop at Y^+ after $\sim$35ps, by exerting a clockwise spin–torque using $\hbar\omega_p$=3.02eV (HH photoholes). A more dramatic demonstration of the flexibility offered by fs spin–orbit torque is given in Fig. 11(d). Here we initiate the $X^+\rightarrow Y^-$ switching as above and then stop it immediately, by applying a control laser–pulse–train at τ=2ps, i.e. long before any oscillations can develop. Instead of relying on the precession phase as in Fig. 10, we apply a sufficiently strong clockwise fs spin–orbit torque that opposes the magnetization motion. In this way, we stop the magnetization at its tracks, after a minimal motion without oscillations. We conclude that coherent optical control of the mobile spin excited during fs laser pulses allows us to suppress both magnetic ringing and nonlinear switching rotations, by controlling the direction, duration, and magnitude of fs spin–orbit torques.

VII. CONCLUSIONS AND OUTLOOK

In this paper we used density–matrix equations of motion with bandstructure to describe photoexcitation and control of fs spin–orbit torques analogous to the static current–induced ones in spintronics. In this all–optical way, we can initiate and control multiple magnetic switchings and magnetic ringing. The proposed non–adiabatic mechanism involves optical control of direction, magnitude, and temporal profile of fs spin–orbit torque sequences. This is achieved by tuning, via the optical field, a short–lived population and spin imbalance between exchange–split bands with different spin–orbit interactions. The photoexcited spin magnitude and direction depend on symmetry–breaking arising from the non–perturbative competition of spin–orbit and spin–exchange couplings of coherent photoholes. We validated our initial prediction of fs spin–orbit torque[3] by comparing our calculations to existing magneto–optical pump–probe measurements, which monitor the very early $\sim$100fs temporal regime following excitation with a single linearly–polarized pulse. The most clear experimental signature is the observation of laser–induced fs magnetic hysteresis and switching of the direction of out–of–plane femtosecond magnetization component with magnetic state. Such magnetic hysteresis is absent without pump, while static planar Hall effect measurements observe similar switchings in the transverse component of the Hall magnetoresistivity. Switching of the direction of the laser–induced fs transverse magnetization with magnetic state cannot arise from longitudinal nonlinear optical effects and demagnetization/amplitude changes. The dependence on magnetic state disappears with increasing perpendicular magnetic field, which suppresses the magnetization re–orientation. In this way we can separate experimentally longitudinal and transverse femtosecond magnetization changes. We discussed two theoretical results that may be useful for coherent control of magnetic memory states and magnetic ringing via fs spin–orbit torque: (i) We showed that femtosecond optical excitation can start, stop, and restart switching pathways between the adiabatic free energy magnetic states in any direction. Based on this, we gave an example of sequences of laser–pulse trains that can provide controlled access to four different magnetic states via consequative 90° switchings, clockwise or counter–clockwise. (ii) We demonstrated optical control of magnon oscillations and switching rotations and suppression of magnetic ringing at any time, long or short. For this we enhance spin–orbit torque via pulse–shaping and control its direction via the frequency.

The model four–state magnetic memory of Fig. 1(b) allows for verifiable tests to determine the feasibility of our fs spin–orbit torque proposal in realistic materials. A full non–thermal control of this four–state memory using our scheme requires the following: (i) The competition between spin–orbit and magnetic exchange interaction breaks the symmetry while the laser electric field couples to the material, so e–h pair excitations can be photoexcited with a finite spin. There is no need to transfer angular–momentum from the photons (no circular polarization of the laser light), since spin–orbit coupling does not conserve spin. (ii) The direction, magnitude, and duration of the non–thermal carrier spin is coherently controlled by the optical field. In particular, the direction of photoexcited spin is controlled by the laser frequency, the magnetic state, and the symmetry–breaking. Importantly, its magnitude increases with laser intensity and $\mathbf{E}^2$, while its temporal profile follows that of the laser pulse if relaxation is faster. Such character-

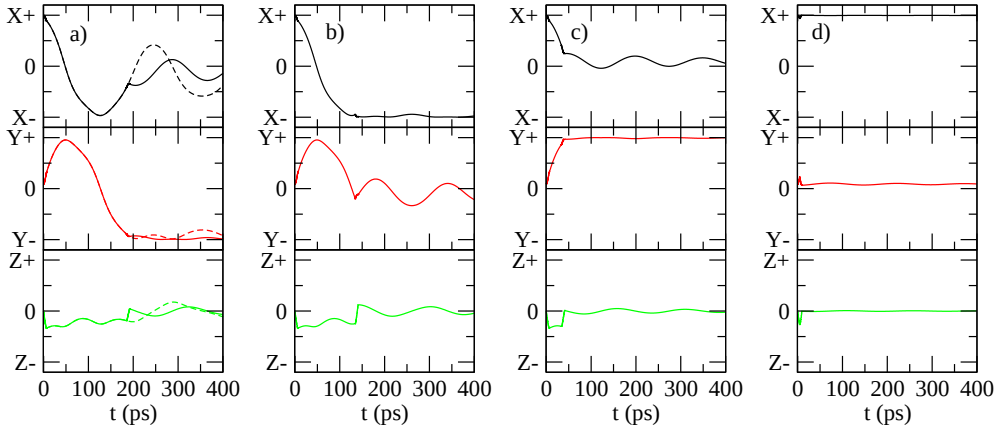

FIG. 11: (Color online) Time–dependence of magnetization components controlled by a time–delayed fs spin–orbit torque pulse train. (a): A $X^+ \rightarrow Y^+ \rightarrow X^- \rightarrow Y^-$ switching pathway is initiated at τ=0 with HH photoexcitation (dashed line). After it completes, the magnetic ringing is reduced with a control laser–pulse–train that exerts opposing fs spin–orbit torques at any time (solid line). (b): $X^+ \rightarrow Y^-$ switching of (a) is terminated via opposing fs spin–orbit torques after magnetization reversal to X^-. (c): $X^+ \rightarrow Y^-$ switching of (a) is terminated via a control laser–pulse–train after 90° rotation to Y^+. (d): $X^+ \rightarrow Y^-$ switching of (a) is stopped immediately after it is initiated, via opposing fs spin–orbit torque at τ=2ps.

istics of fs spin–orbit torque can distinguish it from adiabatic changes. (iii) The photoexcited carrier spin–pulses exert fs spin–orbit–torques on the collective local spin and move it "suddenly", in a controllable direction that depends on the magnetic state and the laser frequency. Important is the pump–induced fs magnetic hysteresis for small magnetic fields, absent in the static Kerr rotation angle without pump. By coherently controlling the non–thermal population imbalance of exchange–split carrier bands with different spin–orbit interactions, we can move the local spin via non–adiabatic interaction with mobile spins. (iv) Laser–pulse–shaping[22] and increased pump–fluence allow us to access optically the magnetic nonlinearities of the carrier free energy. In this way, we may initiate or modify, during fs timescales, deterministic switchings to any available magnetic state. (v) By using control pulse–trains with appropriate frequencies, we suppress and restart switching rotations at intermediate magnetic states and suppress magnetic ringing after switchings complete. While coherent suppression of magnon oscillations is possible by taking advantage of the precession phase, here we mainly relied on controlling the direction of fs spin–orbit torque with respect to the direction of magnetization rotation. In this way we suppressed and enhanced both switching and ringing at long and short times.

To control the entire four–state memory as in Fig. 9, we had to use two time–delayed laser–pulse–trains with different frequencies at each intermediate magnetic state. The first excitation suppresses the switching rotation/ringing in order to access the state, while the second excitation restarts the process and moves the magnetization to the next magnetic state in the desired direction. While such control of the magnetization trajectory occurs on the 100fs timescale of coherent photoexcitation, the initiated deterministic switchings complete on ∼100ps timescales, as determined by the free energy and micromagnetic parameters. In a massively–parallel memory, we can control n different bits simultaneously on the 100fs timescale without waiting for each switching to complete. For large n, this would ideally result in memory reading and writing at ∼10THz speeds.

Our proposed fs spin–orbit torque mechanism may be relevant to different unexplored spin–orbit coupled materials with coexisting mobile and local carriers,[11] for example topological insulators doped with magnetic impurities.[9,10] Important for practical implementations and experimental proof of fs spin–orbit torque is to identify materials where the quasi–thermal/adiabatic and non–thermal/non–adiabatic contributions to the magnetic anisotropy can be distinguished experimentally. It is possible to separate these two based on their temporal profiles and their dependence on photoexcitation intensity, laser frequency, and external magnetic field. In (Ga,Mn)As, Fig. 3 shows photogeneration of a "sudden" magnetization laser–induced re–orientation and fs magnetic hysteresis for magnetic field perpendicular to the sample plane. Such magnetic field cants the ground state magnetization out of the plane, from S_z=0 (B=0) to $S_z \approx \pm S$ (large B). When $S_z \approx 0$ in equilibrium, ΔS_z(t) measures transverse magnetization re–orientation and magnetic hysteresis correlated with in–plane switching, while when $S_z \approx S$ longitudinal changes dominate ΔS_z(t) and there is no hysteresis. In this way, a perpendicular magnetic field can be used to elucidate the physical origin of the fs magneto–optical pump–probe signal dynamics. Distinct thermal and non–thermal contributions to the ps magnetization trajectory were also observed experimentally at $\hbar\omega_p \sim 1.5$eV.[35] They were separated based mainly on pump fluence dependence and by controlling the material's micromagnetic parameters. Qualitative differences in the magnetization trajectory were observed above ∼70

μJ/cm^2 pump fluence. Below this, the easy axis rotates smoothly inside the plane, due to laser–induced temperature increase during ∼10ps timescales.[32,35] Above ∼70 μJ/cm^2, a sub–picosecond "sudden" magnetization component is clearly observed.[32,35] Importantly, while the precession frequency γH_{FS} increases linearly with equilibrium temperature, it saturates with pump fluence above ∼70μJ/cm^2, even though the impulsive out–of–plane magnetization tilt continues to increase.[35] In contrast, the pump–induced reflectivity increases linearly with pump intensity up to much higher fluences ∼150-200μJ/cm^2,[35] which indicates non–thermal photocarriers. At high intensities of 100's of μJ/cm^2, fs demagnetization through dynamical polarization of longitudinal hole spins dominates.[62]

In closing, we note that the discussed concepts are of more general applicability to condensed matter systems. The main idea is the possibility to tailor order parameter dynamics via optical coherent control of non–thermal carrier poulations, as well as via charge fluctuations and interactions driven while the optical field couples to the material. The initial coherent excitation temporal regime may warrant more attention in various condensed matter systems.[1,4] An analogy can be drawn to the well–known coherent control of femtosecond chemistry and photosynthetic dynamics, where the photoproducts of chemical and biochemical reactions can be influenced by creating coherent superpositions of molecular states.[64] Similarly, in condensed matter systems, laser–driven e–h pairs (optical polarization) can tailor non–adiabatic "initial conditions" that drive subsequent phase dynamics governed by the free energy. An analogy can also be drawn to parameter quenches studied in cold atomic gases. "Quasi–instantaneous" quenches drive dynamics that, in some cases such as BCS superconductors, can be mapped to classical spin dynamics. Coherent dynamics of superconducting order parameters are now beginning to be studied in condensed matter systems,[67,68] and an analogy to the magnetic order parameter studied here is clear. Other examples include quantum femtosecond magnetism in strongly–correlated manganites,[1,4] photon–dressed Floquet states in topological insulators,[69] or the existence of non–equilibrium phases in charge–density–wave[47] and other correlated systems. Femtosecond nonlinear optical spectroscopy offers the time resolution needed to disentangle different order parameters that are strongly coupled in the ground state, based on their different dynamics after "sudden" departure from equilibium.[47,48] Multi–pulse switching protocols based on non–adiabatic quantum excitations can control non–equilibrium phase transitions, by initiating phase dynamics in a controllable way.[1,4]

VIII. ACKNOWLEDGEMENTS

This work was supported by the European Union's Seventh Framework Programme (FP7-REGPOT-2012-2013-1) under grant agreement No. 316165, by the EU Social Fund and National resources through the THALES program NANOPHOS, by the Greek Ministry of Education ARISTEIA–APPOLO, and by the National Science Foundation Contract No. DMR-1055352.

Appendix A: Fermi–Dirac/Adiabatic versus Non–thermal/Non–adiabatic Magnetic Anisotropy

In this appendix we discuss the two contributions to laser–induced anisotropy, non–thermal and quasi–thermal. The adiabatic/quasi–thermal contribution comes from relaxed Fermi–Dirac carriers. The non–adiabatic contribution comes from the coherent/non–thermal photoexcited carriers, whose populations increase with intensity during photoexcitation. In the initial stage, these non–thermal carriers come from the continuum of e–h excitations excited by the fs laser pulse, so they follow its temporal profile. At a second stage, they redistribute among the different $\mathbf{k}$ and band states while also scattering with the Fermi sea carriers.

1. Non–thermal/non–adiabatic magnetic anisotropy

We use density matrix equations of motion and bandstructure to describe the femtosecond photoexcitation of short–lived photohole spin–pulses driven by four competing effects: (i) magnetic exchange interaction between local and mobile spins, (ii) spin–orbit coupling of the mobile carriers, (iii) coherent nonlinear optical processes, and (iv) fast carrier relaxation. The interplay of these contributions breaks the symmetry and excites a controllable fs magnetic anisotropy field due to non–thermal photocarriers. The photoexcited spin, Eq.(3), is expressed in terms of the electronic density matrix, which resolves the different band and $\mathbf{k}$–direction contributions. Density matrix equations of motion were derived for the time–dependent Hamiltonian $H(t)$, Eq. (8), with bandstructure treated within standard tight–binding and mean–field approximations. This Hamiltonian has fast and slow contributions. Its adiabatic part $H_b(\mathbf{S}_0)$, Eq. (4), depends on the slowly varying (ps) spin $\mathbf{S}_0$. The eigenstates of $H_b(\mathbf{S}_0)$ describe electronic bands determined by periodic potential, spin–orbit, and adiabatic magnetic exchange couplings. The latter,

$$H_{pd}(\mathbf{S}_0) = \beta c\, \mathbf{S}_0 \cdot \hat{\mathbf{s}}_h, \tag{A1}$$

where $\hat{\mathbf{s}}_h$ is the hole spin operator, leads to exchange–splitting of the HH and LH semiconductor valence bands determined by the exchange energy Δ_{pd}=$\beta c S$. It also modifies the direction of photoexcited spin, by competing with the spin–orbit coupling of the mobile carriers characterized by the energy splitting Δ_{so} of the spin–orbit–split valence band of the parent material (GaAs) at $\mathbf{k}$=0. By adding to the Hamiltonian carrier–carrier and

carrier–phonon interactions, we can also treat relaxation, included here by introducing the non–thermal population relaxation time T_1 and the e–h dephasing time T_2.

We describe the band eigenstates of the adiabatic electronic Hamiltonian $H_b(\mathbf{S}_0)$ by using the semi–empirical tight–binding model that reliably describes the GaAs bandstructure.[51] Compared to the standard $\mathbf{k}\cdot\mathbf{p}$ effective mass approximation, this tight–binding approach allows us to address states with large momenta $\mathbf{k}$. Such anisotropic and non–parabolic band states contribute for laser frequencies away from the band–edge. Following Ref.[51], we include the quasi–atomic spin–degenerate orbitals $3s$, $3p_x$, $3p_y$, $3p_z$, and $4s$ of the two atoms per GaAs unit cell and use the tight–binding parameter values of the Slater–Koster sp^{3}s* model. We add to this description of the parent material the mean–field coupling of the Mn spin, Eq.(A1), which modifies spin–mixing in a non–perturbative way. Similar to Ref.[51], we diagonalize the Hamiltonian $H_b{=}H_b^c{+}H_b^v$ to obtain the conduction (H_b^c) and valence (H_b^v) bands sketched in Fig. 1(a):

$$H_b(\mathbf{S}_0)=\sum_{\mathbf{k}n}\varepsilon^c_{\mathbf{k}n}\,\hat{e}^\dagger_{\mathbf{k}n}\hat{e}_{\mathbf{k}n}+\sum_{\mathbf{k}n}\varepsilon^v_{-\mathbf{k}n}\,\hat{h}^\dagger_{-\mathbf{k}n}\hat{h}_{-\mathbf{k}n}. \quad \text{(A2)}$$

The eigenvalues $\varepsilon^c_{\mathbf{k}n}(\mathbf{S}_0)$ and $\varepsilon^v_{-\mathbf{k}n}(\mathbf{S}_0)$ describe the conduction and valence band energy dispersions.

While $\mathbf{S}_0$ varies on a ps timescale much slower than the laser–induced electronic fluctuations, the rapidly–varying (fs) part of the Hamiltonian $H(t)$, $\Delta H_{exch}(t)+H_L(t)$, drives "sudden" deviations from adiabaticity. $\Delta H_{exch}(t)$, Eq.(9), describes non–adiabatic interactions of photocarrier spins with the fs magnetization $\Delta\mathbf{S}$(t) induced by fs spin–orbit torque. $H_L(t)$ describes the optical field dipole coupling within the rotating wave approximation:

$$H_L(t)=-\sum_{nm\mathbf{k}}d_{nm\mathbf{k}}(t)\,\hat{e}^\dagger_{\mathbf{k}m}\,\hat{h}^\dagger_{-\mathbf{k}n}+h.c, \quad \text{(A3)}$$

where $d_{nm\mathbf{k}}(t)=\mu_{nm\mathbf{k}}\mathcal{E}(t)$ is the Rabi energy, $\mathcal{E}(t)$ is the pump electric field, and $\mu_{nm\mathbf{k}}$ is the dipole transition matrix element between the valence band n and the conduction band m at momentum $\mathbf{k}$. These dipole matrix elements also depend on $\mathbf{S}_0$ and are expressed in terms of the tight-binding parameters of $H_b(\mathbf{k})$ as in Ref.[63]:

$$\mu_{nm\mathbf{k}}=\frac{i}{\varepsilon_{m\mathbf{k}}-\varepsilon_{n\mathbf{k}}}\langle n\mathbf{k}|\nabla_{\mathbf{k}}H_b(\mathbf{k})|m\mathbf{k}\rangle. \quad \text{(A4)}$$

The density matrix $\langle\hat{\rho}\rangle$ obeys the equations of motion

$$i\hbar\frac{\partial\langle\hat{\rho}\rangle}{\partial t}=\langle[\hat{\rho},H(t)]\rangle+i\hbar\frac{\partial\langle\hat{\rho}\rangle}{\partial t}|_{relax}. \quad \text{(A5)}$$

The hole populations and coherences between valence bands are given by the equation of motion

$$\begin{aligned}&i\hbar\,\partial_t\langle\hat{h}^\dagger_{-\mathbf{k}n}\hat{h}_{-\mathbf{k}n'}\rangle-\left(\varepsilon^v_{\mathbf{k}n'}-\varepsilon^v_{\mathbf{k}n}-i\Gamma^h_{nn'}\right)\langle\hat{h}^\dagger_{-\mathbf{k}n}\hat{h}_{-\mathbf{k}n'}\rangle\\&=\sum_m d^*_{mn\mathbf{k}}(t)\,\langle\hat{h}_{-\mathbf{k}n'}\hat{e}_{\mathbf{k}m}\rangle-\sum_m d_{mn'\mathbf{k}}(t)\,\langle\hat{h}_{-\mathbf{k}n}\hat{e}_{\mathbf{k}m}\rangle^*\\&+\beta c\Delta\mathbf{S}\sum_l\left[\mathbf{s}^h_{\mathbf{k}n'l}\langle\hat{h}^\dagger_{-\mathbf{k}n}\hat{h}_{-\mathbf{k}l}\rangle-\mathbf{s}^{h*}_{\mathbf{k}nl}\langle\hat{h}^\dagger_{-\mathbf{k}l}\hat{h}_{-\mathbf{k}n'}\rangle\right], \quad \text{(A6)}\end{aligned}$$

where $n{=}n'$ describes the non–thermal populations and $n{\neq}n'$ the coherent superpositions of different valence band states. $\Gamma^h_{nn}{=}\hbar/T_1$ characterizes the non–thermal population relaxation. $\Gamma^h_{nn'}$ are the inter–valence–band dephasing rates, which are short and do not play an important role here. The first term on the rhs describes the photoexcitation of hole populations in band states $(n,\mathbf{k})$ that depend on $\mathbf{S}_0$. The second term is beyond a simple rate equation approximation and describes the non–adiabatic changes in the hole states induced by their interaction with the rapidly varying (fs) photoinduced magnetization $\Delta\mathbf{S}$(t), Eq.(9). Similarly,

$$\begin{aligned}&i\hbar\,\partial_t\langle\hat{e}^\dagger_{\mathbf{k}n}\hat{e}_{\mathbf{k}n'}\rangle-\left(\varepsilon^c_{\mathbf{k}n'}-\varepsilon^c_{\mathbf{k}n}-i\Gamma^e_{nn'}\right)\langle\hat{e}^\dagger_{\mathbf{k}n}\hat{e}_{\mathbf{k}n'}\rangle=\\&\sum_{m'}d^*_{nm'\mathbf{k}}\langle\hat{h}_{-\mathbf{k}m'}\hat{e}_{\mathbf{k}n'}\rangle-\sum_{m'}d_{n'm'\mathbf{k}}\langle\hat{h}_{-\mathbf{k}m'}\hat{e}_{\mathbf{k}n}\rangle^*, \quad \text{(A7)}\end{aligned}$$

where the rates $\Gamma^e_{nn'}$ characterize the electron relaxation.

In the above equations of motion, the photoexcitation of the carrier populations and coherences is driven by the nonlinear e–h optical polarization $\langle\hat{h}_{-\mathbf{k}n}\hat{e}_{\mathbf{k}m}\rangle$ (off–diagonal density matrix element). This coherent amplitude characterizes the e–h excitations driven by the optical field, which here only exist during the laser pulse since their lifetime T_2 (dephasing time) is short:

$$\begin{aligned}&i\hbar\,\partial_t\langle\hat{h}_{-\mathbf{k}n}\hat{e}_{\mathbf{k}m}\rangle-\left(\varepsilon^c_{\mathbf{k}m}+\varepsilon^v_{\mathbf{k}n}-i\hbar/T_2\right)\langle\hat{h}_{-\mathbf{k}n}\hat{e}_{\mathbf{k}m}\rangle\\&=-d_{mn\mathbf{k}}(t)\,\left[1-\langle\hat{h}^\dagger_{-\mathbf{k}n}\hat{h}_{-\mathbf{k}n}\rangle-\langle\hat{e}^\dagger_{\mathbf{k}m}\hat{e}_{\mathbf{k}m}\rangle\right]\\&+\beta c\Delta\mathbf{S}(t)\cdot\sum_{n'}\mathbf{s}^h_{\mathbf{k}nn'}\,\langle\hat{h}_{-\mathbf{k}n'}\hat{e}_{\mathbf{k}m}\rangle\\&+\sum_{n'\neq n}d_{mn'\mathbf{k}}(t)\,\langle\hat{h}^\dagger_{-\mathbf{k}n'}\hat{h}_{-\mathbf{k}n}\rangle\\&+\sum_{m'\neq m}d_{m'n\mathbf{k}}(t)\,\langle\hat{e}^\dagger_{\mathbf{k}m'}\hat{e}_{\mathbf{k}m}\rangle. \quad \text{(A8)}\end{aligned}$$

The nonlinear contributions to the above equation include Phase Space Filling (first line), transient changes in the non–equilibrium hole states due to the non–adiabatic magnetic exchange interaction ΔH_{exch}(t) (second line), and coupling to h–h (third line) and e–e (fourth line) Raman coherences. The coupled Eqs. (A6), (A7), (A8), and (11) describe photoexcitation of non–thermal carriers modified by the local spin rotation. They were derived in Refs.[3,17] using Hartree–Fock factorization.[13,60]

2. Adiabatic/Fermi–Dirac anisotropy

The equilibrium mobile carriers can be described by Fermi–Dirac populations, $f_{n\mathbf{k}}$, of the eigenstates of the adiabatic Hamiltonian $H_b(\mathbf{S}_0)$, which determine the quasi–equilibrium anisotropy field $\mathbf{H}_{FS}$, Eq. (6).[24,31,35] We simplify this thermal contribution by neglecting any laser–induced changes in carrier temperature and chemical potential, which add to our predicted effects. A laser–induced thermal field $\Delta\mathbf{H}_{FS}$(t) develops indirectly from

fs spin–orbit torque as the net spin of the hole Fermi sea bath adjusts to the new non–equilibrium direction of $\mathbf{S}$(t).[17] As already seen from calculations of magnetic anisotropy that assume a Fermi–Dirac distribution,[6,35] the small ($\sim\mu$eV) free energy differences with $\mathbf{S}$ result in anisotropy fields of the order of 10's of mT. The discrepancies between theory and experiment seem to imply that non–equilibrium distributions that are broad in energy are necessary in order to explain the magnitude of the observed effects.[27] Our time–domain calculation of laser–induced magnetic anisotropy driven by the photoexcited fs population and spin imbalance agrees with experimental measurements. However, we must still include the thermal Fermi sea anisotropy in order to describe the four–state magnetic memory. For this we express the free energy in the experimentally–observed form dictated by symmetry,[6,38,59] also obtained by expanding the theoretical expression:[6]

$$E_h(\mathbf{S}) = K_c(\hat{S}_x^2\hat{S}_y^2 + \hat{S}_x^2\hat{S}_z^2 + \hat{S}_y^2\hat{S}_z^2) + K_{uz}\hat{S}_z^2 - K_u\hat{S}_x\hat{S}_y, \tag{A9}$$

where $\hat{\mathbf{S}}$=$\mathbf{S}/S$ is the unit vector that gives the instantaneous magnetization direction. K_c is the cubic anisotropy constant, K_{uz} is the uniaxial constant, which includes *both strain and shape anisotropies*, and K_u describes an in–plane anisotropy due to strain. We used measured anisotropy parameter values[38] K_c=0.0144meV, K_u=0.00252meV, and K_{uz}=0.072meV. We thus obtain the thermal anisotropy field

$$\gamma\mathbf{H}_{FS} = -\frac{2K_c}{S}\hat{\mathbf{S}} + \frac{1}{S}(2K_c\hat{S}_x^3 + K_u\hat{S}_y,$$
$$2K_c\hat{S}_y^3 + K_u\hat{S}_x, 2K_c\hat{S}_z^3 - 2K_{uz}\hat{S}_z). \tag{A10}$$

The above expression describes the equilibrium magnetic nonlinearities of the realistic material. By expressing $\mathbf{S}$ in terms of the polar angles ϕ and θ, defined with respect to the crystallographic axes, we obtain the easy axes from the condition $\mathbf{S}\times\mathbf{H}_{FS}$=0, by solving the equations

$$2K_c\cos^3\theta - (K_c + K_{uz})\cos\theta + \frac{BS}{2} = 0 \tag{A11}$$

$$\sin 2\phi = \frac{K_u}{K_c\sin^2\theta}, \tag{A12}$$

where we added the external magnetic field B along the [001] direction. For B=0, θ=$\pi/2$ and Eq.(A12) gives the in–plane easy axes of Fig. 1(b). For small K_u, these magnetic states X^+, X^-,Y^+, and Y^- are tilted from the [100] and [010] crystallographic directions by few degrees inside the plane.[32,59] As can be seen from Eq.(A11), the B–field along [001] cants the easy axes out of the plane. In this case, $\theta\neq\pi/2$ and Eq.(A12) shows a simultaneous rotation inside the plane. The above out–of–plane easy axis component, measured by the static Kerr rotation angle $\theta_K(B)$,[34,62] varies smoothly with magnetic field. On the other hand, Eq.(A12) gives two different values for ϕ (X and Y), which can switch due to either B–field changes (as seen in the transverse Hall magnetoresistivity[34]) or laser–induced fs spin–orbit torque (as predicted here).

Appendix B: Band Continuum of Electronic States

The average hole spin $\mathbf{s}_h$(t), Eq.(3), that triggers the fs magnetization dynamics here has contributions $\mathbf{s}^h_{\mathbf{k}n}$(t) from an anisotropic continuum of photoexcited non–parabolic band states. At $\hbar\omega_p\sim$1.5eV, this continuum includes disordered–induced states below the bandgap of the pure semiconductor.[27] At $\hbar\omega_p\sim$3.1eV, photoexcitation of such impurity band/defect states is small, while the almost parallel conduction and valence bands lead to excitation of a wide range of $\mathbf{k}$ states. Integration over the Brillouin zone momenta, as in Eq.(3), presents a well–known challenge for calculating magnetic anisotropies and other properties of real materials.[58] To simplify the problem, one often calculates the quantities of interest at select $\mathbf{k}$–points and replaces the integral by a weighted sum over these "special points" (special point approximation).[58] In our previous work,[3] we considered eight special $\mathbf{k}$–points (Λ–point[7]) along $\{111\}$. While this approximation takes into account the general features of the anisotropic states, it misses important details, such as strong band non–parabolicity, density of states, and photoexcited carrier densities. To compare with the photocarrier densities in the experiment and to address issues such as the frequency dependence of the photoexcited spins, we must include continua of band states in our calculation. Here we integrate over the band–momenta along the eight $\{111\}$ symmetry lines by using the "special lines approximation" discussed in Ref.[66]. At $\hbar\omega_p\approx$3.1eV, we approximate the three–dimensional momentum integral by a sum of one–dimensional integrals along the eight $\mathbf{k}$ directions populated by photoexcited carriers. This simple approximation includes the anisotropic, non–parabolic band continua.[66]

Following Ref.[66], we first express

$$\frac{1}{V}\sum_{\mathbf{k}}\Delta\mathbf{s}^h_{\mathbf{k}} = \frac{1}{(2\pi)^3}\int_{BZ}\Delta\mathbf{s}^h_{\mathbf{k}}\,d\mathbf{k}$$
$$= \int\frac{d\Omega}{4\pi}\left[\frac{1}{(2\pi)^3}\int_0^{k_{BZ}}4\pi k^2dk\Delta\mathbf{s}^h_{\mathbf{k}}\right], \tag{B1}$$

where k_{BZ} is the Brillouin zone boundary and $d\Omega$ is the angular integral. To calculate the above angular–average, we use the special lines approximation[66]

$$\int\frac{d\Omega}{4\pi}\,\Delta\mathbf{s}^h_{\mathbf{k}} = \sum_\alpha w_\alpha\,\Delta\mathbf{s}^h_{k\alpha}, \tag{B2}$$

where α runs over the dominant symmetry directions, k is the wavevector amplitude, and w_α are weight factors. For $\hbar\omega_p\sim$3.1eV, the dominant contribution comes from the eight $\{111\}$ symmetry directions, so we approximate

$$\frac{1}{V}\sum_{\mathbf{k}}\Delta\mathbf{s}^h_{\mathbf{k}} = \frac{1}{(2\pi)^3}\sum_{\alpha=\{111\}}w_\alpha\int_0^{k_{BZ}}4\pi k^2\,\Delta\mathbf{s}^h_{k\alpha}\,dk \tag{B3}$$

Instead of eight discrete $\mathbf{k}$–point populations as in Ref.[3], here we consider continuum distributions along the eight

one–dimensional **k**–lines. While the estimation of optimum weight factors w_α is beyond the scope of this paper,[58] the order of magnitude of the predicted effects is not sensitive to their precise value. We fix w_α=w by reproducing the net photohole density n at one experimentally–measured intensity:

$$n = \frac{1}{V}\sum_{\mathbf{k}}\sum_{n}\Delta\langle\hat{h}^\dagger_{-\mathbf{k}n}\,\hat{h}_{-\mathbf{k}n}\rangle$$
$$= \frac{w}{(2\pi)^3}\sum_{\beta=\{111\}}\int_0^{k_{BZ}} 4\pi k^2\,\Delta\langle\hat{h}^\dagger_{k\beta n}\,\hat{h}_{k\beta n}\rangle. \quad \text{(B4)}$$

For the results of Fig. 3, the photocarrier density $n{\sim}6{\times}10^{18}/\mathrm{cm}^3$ for pump fluence $\sim 7\ \mu J/cm^2$ gives $w{\sim}1/15$. The same order of magnitude of n is obtained, however, for all other reasonable values of w.[66] We then used this weight factor for all other laser intensities.

[1] T. Li *et. al.*, Nature **496**, 69 (2013).
[2] J. A. de Jong *et. al.*, Phys. Rev. Lett. **108**, 157601 (2012).
[3] M. D. Kapetanakis, I. E. Perakis, K. J. Wickey, C. Piermarocchi, and J. Wang Phys. Rev. Lett. **103**, 047404 (2009).
[4] T. Li, A. Patz, P. Lingos, L. Mouchliadis, L. Li, J. Yan, I. E. Perakis, and J. Wang, arXiv:1409.1591 (2014).
[5] C. Chappert, A. Fert, and F. N. Van Dau, Nature Mater. **6**, 813 (2007).
[6] T. Jungwirth *et al*, Rev. Mod. Phys. **78**, 809 (2006); T. Dietl and H. Ohno, Rev. Mod. Phys. **86**, 187 (2014).
[7] K. S. Burch, D. D. Awschalom, and D. N. Basov, J. Magnetism and Magnetic Materials **320**, 3207 (2008).
[8] J. Wang *et al.*, J. Phys. Condes. Matter **18**, R501 (2006).
[9] J. G. Checkelsky, J. Ye, Y. Onose, Y. Iwasa, and Y. Tokura, Nature Physics **8**, 729 (2012).
[10] Y. Fan *et. al.*, Nature Materials **13**, 699 (2014).
[11] E. L. Nagaev, Phys. Rep. **346**, 387 (2001).
[12] J.–Y. Bigot, M. Vomir, & E. Beaurepaire, Nature Physics **5**, 515 (2009); U. Bovensiepen, Nature Physics **5**, 461 (2010); C. Boeglin *et. al.*, Nature **465**, 458 (2010).
[13] F. Rossi and T. Kuhn, Rev. Mod. Phys. **74**, 895 (2002).
[14] D. S, Chemla and J. Shah, Nature **411**, 549 (2001).
[15] S. T. Cundiff and S. Mukamel, Physics Today **66**, 44 (2013).
[16] V. M. Axt and S. Mukamel, Rev. Mod. Phys. **70**, 145 (1998).
[17] J. Chovan, E. G. Kavousanaki, and I. E. Perakis, Phys. Rev. Lett. **96**, 057402 (2006); J. Chovan and I. E. Perakis, Phys. Rev. B **77**, 085321 (2008).
[18] W. S. Fann, R. Storz, H. W. K. Tom, and J. Bokor, Phys. Rev. B **46**, 13592 (1992).
[19] K. H. Ahn, M. J. Graf, S. A. Trugman, J. Demsar, R. D. Averitt, J. L. Sarrao, and A. J. Taylor, Phys. Rev. B **69**, 045114 (2004).
[20] X. Cui *et.al.*, Nature Physics **10**, 505 (2014).
[21] J.H. Mentink, and M. Eckstein, Phys. Rev. Lett. **113**, 057201 (2014).
[22] D. B. Turner, K. W. Stone, K. Gundogdu, and K. A. Nelson, Rev. Sci. Instrum. **82**, 081301 (2011).
[23] R. R. Ernst, G. Bodenhausen, & A. Wokaun, Principles of Nuclear Magnetic Resonance in One and Two Dimensions (Oxford University Press, New York, 1987).
[24] A. V. Kirilyuk *et al*, Rev. Mod. Phys. **82**, 2731 (2010).
[25] P. Nemec *et. al.*, Nature Phys. **8**, 411 (2012).
[26] E. Beaurepaire et. al., Phys. Rev. Lett. **76**, 4250 (1996).
[27] L. Cywiński and L. J. Sham, Phys. Rev. B **76**, 045205 (2007).
[28] J. Wang, C. Sun, J. Kono, A. Oiwa, H. Munekata, L. Cywiski, and L. J. Sham, Phys. Rev. Lett. **95**, 167401 (2005); J. Wang, L. Cywiski, C. Sun, J. Kono, H. Munekata, and L. J. Sham, Phys. Rev. B **77**, 235308 (2008).
[29] C.–H. Lambert, S. Mangin, B. S. D. Ch. D. Varaprasad, Y. K. Takahashi, M. Hehn, M. Cinchetti, G. Malinowski, K. Hono, Y. Fainman, M. Aeschlimann, and E. E. Fullerton, Science **345**, 1337 (2014).
[30] I. Radu *et. al.*, Nature **472**, 205 (2011).
[31] J. Y. Bigot *et. al.*, Chem. Phys. **318**, 137 (2005).
[32] J. Qi *et al.*, Appl. Phys. Lett. **91**, 112506 (2007); Phys. Rev. B **79**, 085304 (2009).
[33] J. Wang *et. al.*, Phys. Rev. Lett. **98**, 217401 (2007).
[34] J. Wang *et. al.*, Appl. Phys. Lett. **94**, 021101 (2009).
[35] N. Tesarova *et. al.*, Nature Photonics **7**, 492 (2013).
[36] G. V. Astakhov *et al.*, Appl. Phys. Lett. **86**, 152506 (2005).
[37] Y. Hashimoto and H. Munekata, Appl. Phys. Lett. **93** (2008).
[38] D. M. Wang *et al.*, Phys. Rev. B **75**, 233308 (2007).
[39] M. D. Kapetanakis and I. E. Perakis, Phys. Rev.Lett. **101**, 097201 (2008); Phys. Rev. B. **78**, 155110 (2008); Phys. Rev. B **75**, 140401 (2007); Phys. Rev. B **73**, 174424 (2006).
[40] C. Thurn *et. al.*, Phys. Rev. B **88**, 161302(R) (2013); Phys. Rev. B **87**, 205301 (2013).
[41] D. E. Reiter, T. Kuhn, and V. M. Axt, Phys. Rev. Lett. **102**, 177403 (2009).
[42] T. Gerrits *et. al.*, Nature **418**, 509–512 (2002)
[43] H. W. Schumacher *et.al.*, Phys. Rev. Lett. **90**, 017201 (2003)
[44] S. Kaka and S. E. Russek, Appl. Phys. Lett. **80**, 2958 (2002)
[45] E. Carpene *et.al.*, Phys. Rev. B **84**, 134425 (2011).
[46] H. W. Schumacher, C. Chappert, P. Crozat, R. C. Souza, P. P. Freitas, and M. Bauer, Appl. Phys Lett. **80**, 3781 (2002).
[47] M. Porer, U. Leierseder, J.-M. Mnard, H. Dachraoui, L. Mouchliadis, I. E. Perakis, U. Heinzmann, J. Demsar, K. Rossnagel, and R. Huber, Nature Materials **13**, 857 (2014).
[48] A. Patz, T. Li, S. Ran, R. M. Fernandes, J. Schmalian, S. L. Budko, P. C. Canfield, I. E. Perakis, and J. Wang, Nature Commun. **5**, 3229 (2014).
[49] M. D. Kapetanakis *et. al.*, Appl. Phys. Lett. **99**, 091111 (2011); J. Opt. Soc. Am. B **29**, A95 (2012).
[50] K. Shen and M. W. Wu, Phys. Rev. B **85**, 075206 (2012); M. W. Wu, J. H. Jiang, and M. Q. Weng, Phys. Rep. **493**, 61 (2010).

[51] P. Vogl *et. al.*, J. Phys. Chem. Solids **44**, 365 (1983).
[52] A. Manchon and S. Zhang, Phys. Rev. B **79**, 094422 (2009).
[53] A. Chernyshov, M. Overby, X. Liu, J. K. Furdyna, Y. Lyanda-Geller, and L. P. Rokhinson, Nature Physics **5**, 656 (2009).
[54] L. Berger, Phys. Rev. B **54**, 9353 (1996).
[55] A. Brataas, A. D. Kent, and H. Ohno, Nature Mater. **11**, 372 (2012).
[56] I. E. Perakis and T. V. Shahbazyan, Surface Science Reports **40**, 1 (2000).
[57] M. E. Karadimitriou, E. G. Kavousanaki, K. M. Dani, N. A. Fromer, and I. E. Perakis, J. Phys. Chem. B **115**, 5634 (2011); M. E. Karadimitriou, E. G. Kavousanaki, I. E. Perakis, and K. M. Dani, Phys. Rev. B **82**, 165313 (2010).
[58] P. E. Blöchl, O. Jepsen, and O. K. Andersen, Phys. Rev. B **49**, 16223 (1994); H. J. Monkhorst and J. D. Pack, Phys. Rev. B **13**, 5188 (1976).
[59] U. Welp, V. K. Vlasko-Vlaskov, X. Liu, J. K. Furdyna and T. Wojotowicz, Phys. Rev. Lett. **90** (2003).
[60] H. Haug and S. W. Koch, Quantum Theory of the Optical and Electronic Properties of Semiconductors, 4th ed. (World Scientific, Singapore, 2004)
[61] S. Mukamel, Principles of Nonlinear Optical Spectroscopy, Oxford U. Press, New York (1995).
[62] A. Patz, T. Li, X. Liu, J. K. Furdyna, I. E. Perakis, and J. Wang, Phys. Rev. B (preprint).
[63] L. C. Lew Yan Voon and L. R. Ram–Mohan, Phys. Rev. B **47**, 15500 (1993).
[64] For example, see P. Brumer and M. Shapiro, Phys. Today **64**, 11 (2011).
[65] See for example I. Bloch, J. Dalibard, and W. Zwerger, Rev. Mod. Phys. **80**, 885 (2008).
[66] P. Enders, Semicond. Sci. Technol. **11**, 187 (1996).
[67] T. Papenkort *et. al.*, Phys. Rev. B **76**, 224522 (2007); Phys. Rev. B **78**, 132505 (2008).
[68] R. Matsunaga and R. Shimano, Phys. Rev. Lett. **109**, 187002 (2012).
[69] Y. H. Wang, H. Steinberg, P. Jarillo-Herrero, and N. Gedik, Science **342**, 453 (2013).